

AD-A240 257



2

PL-TR-91-2057

DESIGN AND OPERATION OF THE GL/OPA MOBILE DOPPLER LIDAR

Patrick J. McNicholl

PhotoMetrics, Inc.
4 Arrow Drive
Woburn, MA 01801-2067

15 March 1991



Scientific Report No. 3

Approved for public release; distribution unlimited.

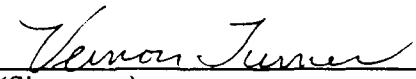



PHILLIPS LABORATORY
AIR FORCE SYSTEMS COMMAND
HANSCOM AFB, MASSACHUSETTS 01731-5000

91-10184

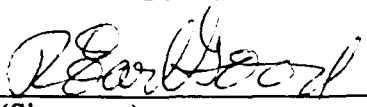


"This technical report has been reviewed and approved for publication"


(Signature)
Vernon Turner
Contract Manager


(Signature)
Donald E. Bedo, Chief
Electro-Optical Measurements Branch

FOR THE COMMANDER


(Signature)
R. Earl Good, SES, Director
Optical Environment Division

This report has been reviewed by the ESD Public Affairs Office (PA) and is releasable to the National Technical Information Service (NTIS).

Qualified requestors may obtain additional copies from the Defense Technical Information Center. All others should apply to the National Technical Information Service.

If your address has changed, or if you wish to be removed from the mailing list, or if the addressee is no longer employed by your organization, please notify GP/IMA, Hanscom AFB, MA 01731. This will assist us in maintaining a current mailing list.

Do not return copies of this report unless contractual obligations or notices on a specific document requires that it be returned.

UNCLASSIFIED

SECURITY CLASSIFICATION OF THIS PAGE

REPORT DOCUMENTATION PAGE

1. REPORT SECURITY CLASSIFICATION UNCLASSIFIED			1b. RESTRICTIVE MARKINGS					
2a. SECURITY CLASSIFICATION AUTHORITY			3. DISTRIBUTION/AVAILABILITY OF REPORT Approved for public release; distribution unlimited.					
2b. DECLASSIFICATION/DOWNGRADING SCHEDULE N/A			5. MONITORING ORGANIZATION REPORT NUMBER(S) PL-TR-91-0057					
4. PERFORMING ORGANIZATION REPORT NUMBER(S)			7a. NAME OF MONITORING ORGANIZATION Phillips Laboratory					
5a. NAME OF PERFORMING ORGANIZATION PhotoMetrics, Inc.		6a. OFFICE SYMBOL (If applicable)		7b. ADDRESS (City, State, and ZIP Code) Hanscom AFB, MA 01731-5000				
5b. ADDRESS (City, State, and ZIP Code) 4 Arrow Drive Webster, MA 01801		9. PROCUREMENT INSTRUMENT IDENTIFICATION NUMBER F19628-86-C-0102						
8a. NAME OF FUNDING/SPONSORING ORGANIZATION		8b. OFFICE SYMBOL (If applicable)		10. SOURCE OF FUNDING NUMBERS				
8c. ADDRESS (City, State, and ZIP Code)		<table border="1"> <tr> <td>PROGRAM ELEMENT NO. 62101F</td> <td>PROJECT NO. 7670</td> <td>TASK NO. 15</td> <td>WORK UNIT ACCESSION NO. AH</td> </tr> </table>			PROGRAM ELEMENT NO. 62101F	PROJECT NO. 7670	TASK NO. 15	WORK UNIT ACCESSION NO. AH
PROGRAM ELEMENT NO. 62101F	PROJECT NO. 7670	TASK NO. 15	WORK UNIT ACCESSION NO. AH					
11. TITLE (Include Security Classification) DESIGN AND OPERATION OF THE GL/OPA MOBILE DOPPLER LIDAR								
12. PERSONAL AUTHOR(S) Patrick J. McNicholl								
13a. TYPE OF REPORT Scientific No. 3		13b. TIME COVERED FROM 870901 TO 900930		14. DATE OF REPORT (Year, Month, Day) 910315				
15. PAGE COUNT 74								
16. SUPPLEMENTARY NOTATION								
17. COSAT CODES			18. SUBJECT TERMS (Continue on reverse if necessary and identify by block number)					
FIELD	GROUP	SUB-GROUP	Lidar Remote Sensing Scattering					
			Doppler Lidar Atmospheric Extinction					
19. ABSTRACT (Continue on reverse if necessary and identify by block number)								
<p>This report covers the theory, design, and operation of the GL/OPA mobile pulsed Doppler lidar facility. This system was constructed for the measurement of atmospheric scattering properties at 10.6 μm as well as eventual measurement of wind velocity. The lidar transmits pulses from a CO₂ TEA laser and uses optical heterodyne techniques to measure both the frequency and amplitude of radiation backscattered by wind-borne aerosols. Detailed discussions are given of the optical layout, alignment procedures, detector performance, design and operation of the receiver electronics, and calibration procedures. A preliminary system performance evaluation is made based on the data collected during the GABLE field measurement program.</p>								
20. DISTRIBUTION/AVAILABILITY OF ABSTRACT <input type="checkbox"/> UNCLASSIFIED/UNLIMITED <input checked="" type="checkbox"/> SAME AS RPT <input type="checkbox"/> OTIC USE ONLY			21. ABSTRACT SECURITY CLASSIFICATION UNCLASSIFIED					
22a. NAME OF REPORTING INDIVIDUAL Mr. Thomas Garrett, Contract Manager			22b. TELEPHONE (Include Area Code) 22c. OFFICE SYMBOL 617/3773662 PL/OPA					

TABLE OF CONTENTS

1. Introduction	1
2. System Modeling Calculations	3
2.1 Definitions and Units	3
2.2 State Vector Formalism and Dirac Notation	5
2.3 Heterodyne Signal and Noise Formulas	7
2.4 Derivation of the Lidar Equation	10
2.5 Modeling of the Lidar Overlap	15
3. Sensitivity Calculations	17
3.1 Beam Sizes and Overlaps	17
3.2 Optics Transmission	17
3.3 Atmospheric Transmission	19
3.4 Target Reflectivity	20
3.5 System Performance	23
4. CO ₂ Laser and Transceiver Optics	25
4.1 Initial Laser Alignments	28
4.1.1 CW Laser	28
4.1.2 TEA Laser	29
4.2 Injection Locking	30
4.2.1 Seed Beam Alignment	30
4.2.2 AFC Pickoff Alignment	30
4.2.3 Injection Locked Operation	30
4.3 Transmit/Receive Optical Alignment	31
4.3.1 Initial HeNe Alignment	31
4.3.2 LO Alignment	32
4.3.3 Final T/R Alignment	33
5. Receiver Electronics	34
5.1 Detector and Bias Circuitry	34
5.2 Detector/Preamp Circuits	36
5.3 High Gain Amplifier and IF Electronics	42
5.4 Aerosol Signal Processing and Electronic Calibration	53
5.5 Utility/Alignment Pyroelectric Detectors	57

6. Calibration Procedures	60
6.1 Field Techniques	60
6.2 Preliminary Data Reduction	62
References	66

LIST OF ILLUSTRATIONS

Figure 1.1	Illustration of lidar heterodyne operation.	2
Figure 4.1	Schematic of Transmitter/Receiver Optics.	26
Figure 4.2	Optical Table Modifications.	27
Figure 5.1.1	Bias Scheme for HgCdTe Detectors.	35
Figure 5.1.2	Schematic of bias test circuit.	37
Figure 5.1.3	Illustration of the use of the bias test circuit to monitor chopped CW signals.	38
Figure 5.2.1	Detector/Preamp Noise model.	39
Figure 5.2.2a	Schematic of Preamp/Bias circuit ($I_B \approx 1\text{mA}$).	43
Figure 5.2.2b	Schematic of Preamp/Bias circuit ($I_B \approx 0.5\text{mA}$).	44
Figure 5.3.1a	Block schematic of Amplifier Unit.	46
Figure 5.3.1b	Amplifier unit: RF module layout.	47
Figure 5.3.1c	Amplifier unit: front panel schematic.	48
Figure 5.3.1d	Amplifier unit: rear panel layout.	49
Figure 5.3.1e	Amplifier unit: switching and MGC board schematic.	50
Figure 5.3.1f	Amplifier unit: power supply circuitry.	51
Figure 5.3.2	Amplifier unit: dual gain ramp operation.	54
Figure 5.4.1	Block Diagram of receiver and data acquisition scheme.	55
Figure 5.4.2	RF detector calibration.	56
Figure 5.5.1	Schematic of the handheld proportional output detector.	58
Figure 5.5.2	Schematic of the audio/visual handheld detector.	59
Figure 6.1.1	Sample target return data (AU210001)	61
Figure 6.2.1	Reduced target return data: IF power versus range.	63
Figure 6.2.2	Reduced horizontal lidar run.	65



Accession For	
NTIS GRA&I	<input checked="" type="checkbox"/>
DTIC TAB	<input type="checkbox"/>
Unannounced	<input type="checkbox"/>
Justification	
By _____	
Distribution/	
Availability Codes	
Dist	Avail and/or Special
A-1	

1. INTRODUCTION

This report covers the work done by PhotoMetrics on the GL/OPA CO₂ lidar system including optics and electronics design and construction, data acquisition hardware and software, testing and operational procedures, system modeling, field support and preliminary data reduction for the SABLE 89 (Ascension Isl.) and GABLE (Azores) field measurement programs.

A block diagram of the lidar illustrating its operation is given in figure 1.1. The transmitted radiation is a train of near Fourier limited pulses with a wavelength of 10.6 μm and derived from an injection locked CO₂ TEA laser operating on the P(20) transition. The characteristics of this laser are listed in table 1.1. Reception is coaxial with transmission and via a 25x, eccentric pupil, Mersenne telescope/beam expander. As shown in figure 1.1, the transmitted and received radiation are separated by a polarizing beam splitter and quarter wave retarder combination. The transmitted light is therefore circularly polarized with the receiver sensitive to circularly polarized backscatter of the opposite sense. The receiver employs a heterodyne detection scheme in which the Doppler shifted light backscattered by aerosols is superimposed at the detector surface with that from a local oscillator (LO) which operates at a fixed frequency offset (40 MHz) from the transmit laser. The resulting intermediate frequency (IF) beat in the detector current is amplified and processed according to the desired mode of operation. In "intensity" mode, the photocurrent power within a bandpass (B) about the carrier frequency is recorded versus time of flight. The resulting waveform is proportional to the received backscattered power versus range. In "complex amplitude" mode the IF waveform is transformed electronically to a two component baseband signal which is processed to yield both signal amplitude and frequency versus time. From these, the received power can be obtained as well as the radial component of the wind velocity. In the initial operation and testing of this lidar only the "intensity" operational mode has been used.

In the following sections, we discuss the modeling, sensitivity, and calibration of the system first and then proceed to the details of the lidar layout, alignment, and electronics.

Table 1.1
CO₂ Laser Operating Parameters

wavelength	10.6 μm
energy/pulse	100 mJ
pulse duration	1-2 μsec
rep. rate	10-100 Hz
spatial mode	TEM00
e ⁻² beam width	3.2 mm
spectral width	≤ 500 kHz
spectral jitter	≈ 1 MHz

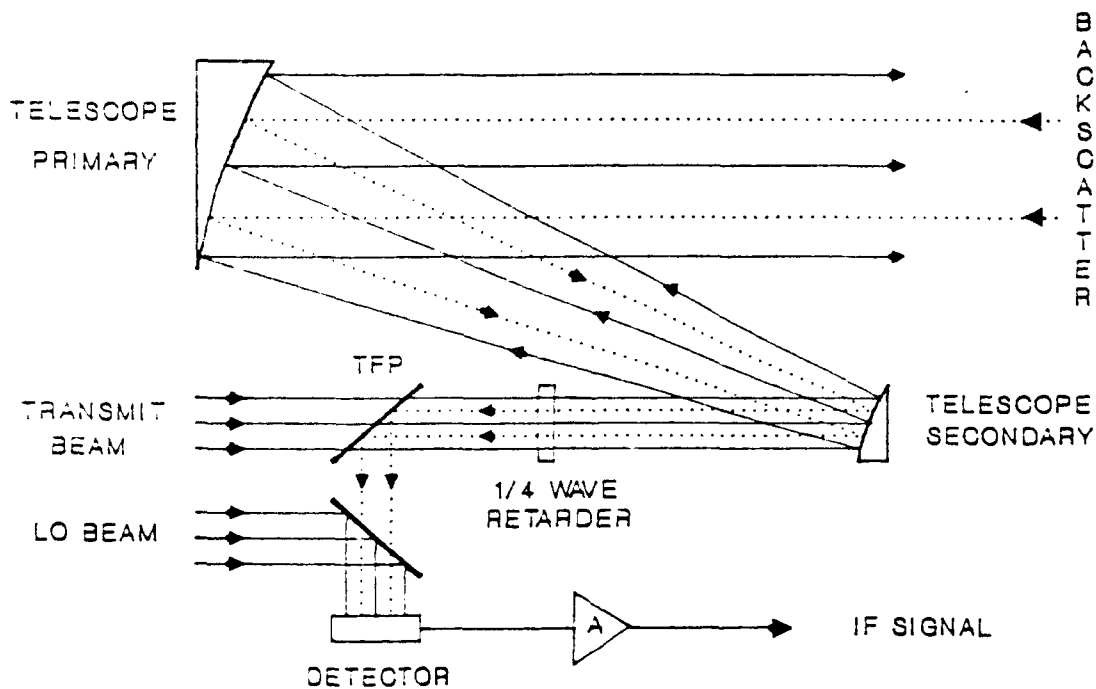


Figure 1.1 Illustration of lidar heterodyne operation.

2. SYSTEM MODELING CALCULATIONS

For the evaluation of system performance as well as calibration, an analysis of expected signal response versus range as well as its dependence on the wavefront properties of the transmitted beam and the LO is needed. A complete derivation of the "lidar equation" for this system is given below. We have found such an *ab initio* treatment necessary to fully appreciate the importance of all the physical assumptions made as well as to provide a unified framework for modifications should the system performance be deemed to be insufficiently approximated by the typically assumed idealized conditions, e.g., diffraction limited optical performance and negligible turbulence. Although the treatment given below is generally equivalent to that in the literature [2.1], we adopt a formalism and notation for the wavefront analysis which simplifies the resulting expressions and makes more transparent their physical interpretation.

2.1 Definitions and Units

For convenience, we adopt units for the electric field (E) such that its square (defined to be the field intensity) has units of W/cm². The spatial dependence of the field for several types of sources is presented below.

(i) Gaussian Beam:

The radial (ρ) dependence of the field for a Gaussian beam in a plane perpendicular to the propagation direction is given by

$$(2.1.1) \quad E(\rho) = A (2/\pi w^2)^{1/2} \exp\{-\rho^2/w^2\} \exp\{-ik\rho^2/2R\}$$

where w is the so-called e^{-2} beam radius, R is the wavefront curvature, and $k=2\pi/\lambda$. $|A|^2$ is the beam power in Watts. If z is the distance from the beam waist to the plane, then the radius $w \equiv w_z$ and curvature $R \equiv R_z$ are given by the standard formulas [2.2]:

$$(2.1.2a) \quad w_z^2 = w_0^2 [1 + (2z/kw_0^2)^2]$$

$$(2.1.2b) \quad R_z = z [1 + (kw_0^2/2z)^2].$$

In these expressions, w_0 is the minimum beam radius.

(ii) Isotropic Point Source:

The field at a distance r from an isotropic point source is given by:

$$(2.1.3) \quad E(r) = A e^{ikr} / r(4\pi)^{1/2}$$

where $|A|^2$ is the total power emitted by the source (W).

(iii) Aerosol Backscatter:

As long as the receiver subtends a small enough angle at the particle so that the differential backscatter coefficient is constant over the entrance aperture, the field due to the backscattered radiation from a single aerosol particle can be taken as that due to an isotropic point source with

$$(2.1.4) \quad |A|^2 = 4\pi I_0 \partial\sigma/\partial\Omega_{180}.$$

Here, I_0 is the incident radiation intensity at the particle (W/cm^2) and $\partial\sigma/\partial\Omega_{180}$ is the differential backscatter cross-section (cm^2/sr). The atmospheric backscatter coefficient (β) is defined loosely to be the average backscatter cross section times the aerosol density. More rigorously

$$(2.1.5) \quad \beta = \int da N(a) \partial\sigma/\partial\Omega(a)$$

where $N(a)$ is the density of aerosols with radius a . If the treatment is to include irregularly shaped particles, the integral over a is assumed to implicitly include averaging over particle shape as well as orientation. Moreover, $\partial\sigma/\partial\Omega$, and therefore β , is implicitly dependent on the polarization of the transmitted beam as well as the polarization state to which the receiver is sensitive (see section 3.4).

2.2 State Vector Formalism and Dirac Notation

The paraxial approximation to the wave equation is valid for the conditions under which this as well as most lidar systems operate. Briefly, only rays originating near and with small inclinations to the transmit/receive (i.e., optic) axis need be treated. The paraxial approximation utilizes this to reduce the second order wave equation for the electric field to one which is first order in the longitudinal coordinate (i.e., the one which measures distance along the optic axis--z). D. Stoler has shown [2.3] that the resulting equation for the propagation of the field is equivalent to the Schroedinger equation with the propagation coordinate z playing the role of time.

It is natural then to employ the standard Dirac bra-ket notation [2.4] and represent the field in the x-y plane at z by a state vector $|E(z)\rangle$. The coordinate representation of this state, $E(x,z)$ as used in section 2.1, is related to this state by:

$$E(x,z) = \langle x | E(z) \rangle,$$

where $|x\rangle$ is the coordinate state vector which is an eigenvector of the two dimensional transverse coordinate

operator $x=(x,y)$, $\langle x|$ is the adjoint state to $|x\rangle$, and $\langle A | B \rangle$ represents the inner product of two state vectors. Since this coordinate state representation is complete and orthogonal, the following identities hold:

$$\begin{aligned} \langle x | x' \rangle &= \delta^{(2)}(x-x') \\ 1 &= \int dx |x\rangle \langle x|. \end{aligned}$$

where $\delta^{(2)}(x)$ is the Dirac delta function. Using these relations, the inner product of the states representing two fields can be shown to be the overlap integral of the fields:

$$\begin{aligned} \langle E_1 | E_2 \rangle &= \langle E_1 | \left\{ \int dx |x\rangle \langle x| \right\} | E_2 \rangle \\ &= \int dx \langle E_1 | x \rangle \langle x | E_2 \rangle \\ &= \int dx E_1^*(x) E_2(x). \end{aligned}$$

and with the unit definitions above $\langle E | E \rangle$ is power of the beam wavefront represented by $|E\rangle$.

Propagation of a wavefront along the z-axis is effected by a unitary operator, $P(z', z)$ which is formally equivalent to the evolution operator in quantum mechanics:

$$|E(z')\rangle = P(z', z) |E(z)\rangle.$$

For propagation in free space or in an isotropic and homogeneous media, the propagator is spatially stationary and given by

$$(2.2.1) \quad P_0(z) = e^{ikz} \exp\{-izp^2/2k\}$$

where \mathbf{p} , the "momentum" operator, has a coordinate space representation:

$$\mathbf{p} = -i\nabla = -i(\partial/\partial x, \partial/\partial y).$$

Propagation by this operator can be shown to be equivalent to the Fresnel diffraction integral

$$E(\mathbf{x}, z) = (1/i\lambda z) \int d\mathbf{x}' e^{ikz} \exp\{ik(\mathbf{x}-\mathbf{x}')^2/2z\} E(\mathbf{x}', 0).$$

and also to yield the standard Gaussian beam formulas discussed in section 2.1.

The representation in this formalism of the fields discussed in the previous section is straightforward. The transverse dependence of a Gaussian TEM_{00} beam at its waist is identical to the ground state wave function for a two dimensional (x-y) quantum mechanical harmonic oscillator with unit mass and a frequency of $2/w_0^2$. We represent this field by $|00\rangle$ indicating that both oscillators are in their ground state. Higher order transverse modes of a stable cavity-- TEM_{nm} --are similarly related to the excited states of the oscillator-- $|nm\rangle$. It was in fact for the modal analysis of stable cavities that this quantum mechanical formalism was originally adopted for the treatment of electric field wavefront propagation.

Under paraxial conditions, the field at (\mathbf{x}, z) due to a point source at $(\mathbf{x}_0, z=0)$ can be written

$$E_p(\mathbf{x}, z) = A e^{ikz} \exp\{ik(\mathbf{x}-\mathbf{x}_0)^2/2z\}/z(4\pi)^{1/2}.$$

This can be obtained from the Fresnel integral equation above with

$$E_p(\mathbf{x}', 0) = i\lambda A \delta^{(2)}(\mathbf{x}' - \mathbf{x}_0).$$

Since $\langle \mathbf{x} | \mathbf{x}' \rangle \equiv \delta^{(2)}(\mathbf{x} - \mathbf{x}')$, the state of the field in the plane of the source can be taken as

$$(2.2.2) \quad |E_p(z=0)\rangle = [i\lambda A/(4\pi)^{1/2}] |x_0\rangle.$$

With a redefinition of A as discussed in section 2.1, this also is the state of the field resulting from backscatter from a single aerosol particle.

2.3 Heterodyne Signal and Noise Formulas

The total electric field at the detector surface (E) is the superposition of the LO field (E_{LO}) and that due to the received backscatter (E_S):

$$|E\rangle = \exp\{-i\omega_S t\} |E_S^{(d)}\rangle + \exp\{-i\omega_{LO} t\} |E_{LO}^{(d)}\rangle,$$

where the superscript indicates evaluation at the detector surface and ω_{LO} (ω_S) is the angular frequency of the signal (LO) field. These frequencies are related to the transmitted radiation frequency (ω_T) by

$$\omega_{LO} = \omega_T + \omega_C$$

and

$$\omega_S = \omega_T + \omega_D.$$

In these expressions, ω_C is the offset (carrier) frequency between the LO and transmitted light and ω_D is the Doppler shift given by

$$\omega_D = -4\pi v/\lambda$$

where v is the radial velocity of the scattering particle measured positively away from the receiver.

The photocurrent induced by this field is

$$i = (\eta q/h\nu) \langle E | E \rangle$$

where η is the photodiode quantum efficiency, q is the electronic charge, and $h\nu$ is the photon energy. This can be rewritten as

$$i = i_{LO} + i_B + i_{IF}$$

where i_{LO} (i_B) is the dc current due to the LO (backscattered) field and i_{IF} is the current at the intermediate frequency $\omega_{IF} = \omega_C - \omega_D$:

$$i_{LO} = (\eta q/h\nu) \langle E_{LO} | E_{LO} \rangle = (\eta q/h\nu) P_{LO}$$

$$i_B = (\eta q/h\nu) \langle E_S | E_S \rangle = (\eta q/h\nu) P_S$$

$$i_{IF} = (\eta q/h\nu) [\langle E_S | E_{LO} \rangle \exp\{i\omega_{IF}t\} + \text{c.c.}]$$

P_{LO} (P_S) is the LO (received backscatter) power incident on the detector (i.e., $\langle E_{LO} | E_{LO} \rangle$) and c.c. stands for the complex conjugate of the previous expression in brackets.

In conventional lidar receivers, there is no LO field and the signal current-- i_B --which is proportional to the power of the backscattered radiation is the measured quantity; no frequency information is obtained (unless spectral filtering of the received backscatter is performed). An optical heterodyne receiver measures the IF current so

that both amplitude and frequency information are obtainable; the dc signal component, i_B , is usually negligible. The IF signal power at ω_{IF} is then

$$(2.3.1) \quad p_{IF} = 2 R_L (\eta q / h\nu)^2 \left| \langle E_{LO}^{(d)} | E_S^{(d)} \rangle \right|^2$$

where R_L is the resistive load on the photodiode--e.g., the input impedance of the preamp--and is assumed small compared to the diode output impedance. It is convenient for this and the following derivations to employ normalized field states $|\epsilon\rangle$ defined by

$$|\epsilon\rangle = |E\rangle / \langle E | E \rangle^{1/2}$$

so that

$$\langle \epsilon | \epsilon \rangle = 1.$$

In terms of this representation, the formula for the IF signal power becomes more explicitly dependent on the LO and received signal power:

$$(2.3.2) \quad p_{IF} = 2 R_L (\eta q / h\nu)^2 P_{LO} P_S \left| \langle \epsilon_{LO}^{(d)} | \epsilon_S^{(d)} \rangle \right|^2.$$

From this expression, it is seen that the IF signal power is proportional to LO power. Therefore the IF power and hence the signal to noise ratio (SNR) increases with increasing LO power until the shot noise due to the dc LO current (i_{LO}) dominates all other sources of noise (e.g., detector and/or added preamplifier noise). The shot noise power in any bandpass B is given by [2.5]:

$$(2.3.3) \quad p_{SN} = 2qBR_L i_{LO} = 2qBR_L (\eta q / h\nu) P_{LO}.$$

The ratio of p_{IF} to p_{SN} yields the SNR for heterodyne operation in the shot noise limited regime:

$$(2.3.3) \quad SNR = \eta P_S \left| \langle \epsilon_{LO}^{(d)} | \epsilon_S^{(d)} \rangle \right|^2 / h\nu B.$$

$$= \eta_{\text{HET}} \eta P_S / h\nu B$$

where η_{HET} is the so-called heterodyne efficiency:

$$\eta_{\text{HET}} = | \langle \epsilon_{\text{LO}}^{(d)} | \epsilon_S^{(d)} \rangle |^2.$$

2.4 Derivation of the Lidar Equation

We have implicitly assumed in the previous section that the detector surface is large enough to subsume the LO and/or the signal field. If this were not the case, then the overlap $\langle E_{\text{LO}}^{(d)} | E_S^{(d)} \rangle$ should be replaced by $\langle E_{\text{LO}}^{(d)} | \Pi_d | E_S^{(d)} \rangle$ where Π_d is a projection operator onto just that portion of the x-y plane occupied by the detector:

$$\Pi_d = \int_d dx | \mathbf{x} \rangle \langle \mathbf{x} |$$

and \int_d indicates that the integral is restricted to the detector surface. The heterodyne efficiency then becomes

$$\begin{aligned} \eta_{\text{HET}} &= | \langle \epsilon_{\text{LO}}^{(d)} | \Pi_d | \epsilon_S^{(d)} \rangle |^2 \\ &= | \int_d dx \epsilon_{\text{LO}}(\mathbf{x})^* \epsilon_S(\mathbf{x}) |^2. \end{aligned}$$

If either E_{LO} or E_S is negligible outside the area occupied by the detector the integration can be performed over the entire plane and the former result obtains. We assume this to be the case.

Under these conditions, it is not necessary or even convenient to evaluate the overlap integral at the detector surface. For example, the fields at the detector can be obtained by propagating those exiting the focusing lens to the detector surface, so that

$$| E_S^{(d)} \rangle = P_0(z_{ld}) | E_S^{(l)} \rangle$$

$$| E_{\text{LO}}^{(d)} \rangle = P_0(z_{ld}) | E_{\text{LO}}^{(l)} \rangle$$

where $P_0(z)$ is the propagation operator as discussed above, z_{ld} is the distance from the lens to the detector, and the l superscript indicates the fields at the lens. Since the propagation operator is unitary, $P_0^\dagger P_0 = 1$ and

$$\begin{aligned} \langle E_{LO}^{(d)} | E_S^{(d)} \rangle &= \{ \langle E_{LO}^{(l)} | P_0(z_{ld})^\dagger \} \{ P_0(z_{ld}) | E_S^{(l)} \rangle \} \\ &= \langle E_{LO}^{(l)} | E_S^{(l)} \rangle, \end{aligned}$$

the overlap can be evaluated after the lens. Since the transformation of a wavefront by a lens consists of just a multiplication by a transversely dependent phase factor, it too can be represented by a unitary operator so that the above evaluation may be performed before the lens. In fact except for element transmission losses, propagation through the entire transmit/receive optical system can be represented by a single unitary operator as long as there is negligible vignetting of the received radiation and/or the virtual LO beam. By virtual beam, we mean that obtained by propagating the LO beam backward through the beam splitter and into the receiver leg as if it were arriving coaxially with the received backscatter radiation. This is sometimes referred to as the backward propagated local oscillator or BPLO [2.1]. Thus we can write

$$| \langle \epsilon_{LO}^{(d)} | E_S^{(d)} \rangle |^2 = T_R | \langle \epsilon_{LO}^{(a)} | E_S^{(a)} \rangle |^2$$

where the superscript a indicates evaluation of the field wavefront at the telescope entrance aperture and T_R is the receiver transmission, i.e., the product of the transmissivity/reflectivity of all of the optical elements of the receiver. Note that we have chosen to employ the full signal field in this expression while for convenience only the normalized virtual LO field is treated and, for its evaluation, transmission losses are to be ignored.

This procedure can be carried further with the fields being propagated out to the actual scattering volumes. To illustrate this, consider the signal due to a point scatterer at a range z_p and a transverse position x_p . Propagating the fields out to the plane containing this particle, we obtain for the overlap:

$$\begin{aligned}
| \langle \epsilon_{LO}^{(d)} | E_S^{(d)} \rangle |^2 &= T_R T_A(z_p) | \langle \epsilon_{LO}^{(p)} | E_S^{(p)} \rangle |^2 \\
&= T_R T_A(z_p) (\partial \sigma / \partial \Omega) \lambda^2 I_0 | \langle \epsilon_{LO}^{(p)} | x_p \rangle |^2.
\end{aligned}$$

In this expression, $T_A(z_p)$ is the atmospheric transmission from the lidar out to the range z_p and the expression for the field due to a point scatterer from section 2.2 has been used. The incident intensity at the particle, I_0 , is given by

$$I_0 = | \langle x_p | E_T^{(p)} \rangle |^2$$

where $| E_T^{(p)} \rangle$ is the field at range z_p due to the transmitted lidar pulse. Using the atmospheric (T_A) and lidar transmitter transmission (T_T) as well as the TEA laser output power (P_T), we can write this as

$$I_0 = T_T T_A(z_p) P_T | \langle x_p | \epsilon_T^{(p)} \rangle |^2,$$

so that the expression for the overlap is explicitly symmetrical in the transmitted pulse and the virtual LO fields:

$$\begin{aligned}
| \langle \epsilon_{LO}^{(d)} | E_S^{(d)} \rangle |^2 &= P_T T_R T_T T_A^2(z_p) (\partial \sigma / \partial \Omega) \lambda^2 \\
&\cdot | \langle \epsilon_{LO}^{(p)} | x_p \rangle \langle x_p | \epsilon_T^{(p)} \rangle |^2.
\end{aligned}$$

Using this in the formulas from the previous section, we obtain for the IF signal power (referred to the input of the preamp) expected from backscatter off a single aerosol particle at range z_p and transverse position x_p :

$$\begin{aligned}
P_{IF}(x_p, z_p, t) &= 2R_L(\eta q / h\nu)^2 P_{LO} P_T(t-2z_p/c) T_R T_T T_A^2(z_p) \\
&\cdot (\partial \sigma / \partial \Omega) \lambda^2 \cdot | \langle \epsilon_{LO}^{(p)} | x_p \rangle \langle x_p | \epsilon_T^{(p)} \rangle |^2.
\end{aligned}$$

Note that the temporal dependence is due solely to that of the laser pulse power and the range (z) and transverse spatial dependence--other than that due to atmospheric extinction--arises from the term:

$$\begin{aligned}
f(x,z) &\equiv \left| \langle \epsilon_{LO}^{(p)} | x \rangle \langle x | \epsilon_T^{(p)} \rangle \right|^2 \\
&= \left| \langle \epsilon_{LO}^{(a)} | P(z, z_a)^\dagger | x \rangle \langle x | P(z, z_a) | \epsilon_T^{(a)} \rangle \right|^2 \\
&= \left| \epsilon_{LO}(x,z) \epsilon_T(x,z) \right|^2
\end{aligned}$$

where $P(z, z_a)$ is the propagator from the telescope aperture to the range z and $\epsilon_{LO}(x,z)$ ($\epsilon_T(x,z)$) is the normalized virtual LO (laser) field at this range. We do not employ the free space propagator $P_0(z-z_a)$ as atmospheric turbulence may significantly alter the propagated wavefronts. In principle the effects of turbulence are to be included in the definition of the propagator.

For convenience, we define the calibration constant A :

$$(2.4.1) \quad A = 2R_L(\eta q/h\nu)^2 P_{LO} T_R T_T \lambda^2.$$

Then in terms of this the IF signal due to a single aerosol is:

$$(2.4.2) \quad p_{IF}(x_p, z_p; t) = A P_T(t-2z_p/c) T_A^2(z_p) (\partial\sigma/\partial\Omega) f(x_p, z_p)$$

and that due to a collection of aerosols at $\{(x_i, z_i)\}$ is

$$p_{IF}(t) = A \sum_i P_T(t-2z_i/c) T_A^2(z_i) (\partial\sigma/\partial\Omega)_i f(x_i, z_i).$$

By passing to the limit

$$\sum_i (\partial\sigma/\partial\Omega)_i \rightarrow \int dx \int dz \beta(z),$$

we obtain for the expected signal due to atmospheric aerosol backscatter:

$$(2.4.3) \quad p_{IF}(t) = A \int dz P_T(t-2z/c) T_A^2(z) \beta(z) F(z),$$

where

$$(2.4.4) \quad F(z) \equiv \int dx f(x,z). \\ = \int dx \left| \epsilon_{LO}(x,z) \epsilon_T(x,z) \right|^2.$$

Equation 2.4.3 is essentially the lidar equation

If backscatter from a calibration target at a range z_T is being measured, equation 2.4.3 can be used with

$$\beta = \rho^* \delta(z-z_T),$$

where ρ^* is the target material's backscatter reflectivity, i.e. the fraction of incident light scattered by the target at 180° per steradian and under the prevailing incidence and polarization conditions. The expected signal power for hard target calibration is then

$$(2.4.5) \quad p_C(t) = A \rho^* P_T(t-2z_T/c) T_A^2(z_T) F(z_T).$$

For calibration purposes, it is more appropriate to use the time integral of this power or the energy of the 1F pulse due to return from the target referred to the preamp input:

$$(2.4.6) \quad e_C = A \rho^* e_T T_A^2(z_T) F(z_T).$$

where e_T is the laser pulse energy. With e_C known, the constant A can be eliminated from the lidar equation if: ρ^* is adequately known; the atmospheric transmission to the target and back is measured or accurately modeled; and the overlap integral $F(z)$ is known. Although only an explicit range dependence for T_A and $F(z)$ is shown, these quantities are implicitly path dependent and their values even at the same range can vary markedly with zenith angle. For the atmospheric transmission, this variation with zenith angle arises mostly from the fall off with altitude of the atmospheric water vapor content which is the dominant source of extinction at $10.6 \mu m$ at low altitudes. The variation of the overlap with zenith angle is probably less drastic but also more uncertain as it arises from the altitude dependence of the atmospheric turbulence.

2.5 Modeling of the Lidar Overlap

The function $F(z)$ as defined in equation 2.4.4 is the overlap integral of the normalized transmitted laser intensity and the virtual LO intensity at range z . The former defines the irradiated area at this range and the latter the transverse dependence of the receiver's sensitivity. $F(z)$ has units of inverse area and can be qualitatively interpreted as the inverse of the area sampled by the lidar system at range z . No coherent effects are evidenced in its definition (eq. 2.4.4) because we have referred the calculation to the plane of the scatterers and there is no correlation in the phases of the backscatter radiation arising from different particles. Thus $F(z)$ is only dependent on the intensities of the fields in this plane. As seen in the previous section, calculation of the overlap in any other plane, e.g. the telescope entrance aperture or the detector plane, results in apparent coherent effects, i.e., field dependence. This results from the partial coherence in the backscattered field arising from propagation [2.6].

The evaluation of $F(z)$ requires two steps: (i) model the transmitted and LO wavefronts at, say, the telescope entrance/exit aperture and (ii) model the atmospheric propagation as a function of range. The former should include any vignetting or aberration in the transmitter/receiver optics and the latter the effects of turbulence on the propagated wavefronts. In this preliminary study, we will neglect these effects effectively adopting the free space propagator $P_0(z)$ as defined in equation 2.2.1.

The ideal case which most closely approximates the characteristics of the GL/OPA CO₂ lidar is that in which the transmitter and LO are Gaussian TEM₀₀ modes. We shall assume for the initial study that these wavefronts are well matched and collimated at the exit aperture of the telescope. In this case, a simple calculation gives:

$$(2.5.1) \quad F(z) = 1/\pi w_z^2$$

where w_z is the Gaussian beam width at range z as given in equation 2.1.2a and the beam waist radius, w_0 , to be used is the e^{-2} radius at the telescope aperture. Using equation 2.1.2a, this can be rewritten as:

$$(2.5.2) \quad F(z) = (1/\pi w_0^2) [1 + (z/z_0)^2]^{-1}$$

where z_0 is sometimes referred to as the Fresnel or diffraction distance and is defined by

$$(2.5.3) \quad z_0 = kw_0^2/2 = \pi w_0^2/\lambda.$$

It is at this distance, z_0 , from the waist that the width of a Gaussian beam has increased by a factor $\sqrt{2}$. It is at this distance that the ideal lidar's sensitivity has fallen by a factor of two from its near field ($z \ll z_0$) value. For ranges such that $z \gg z_0$, the far field, the inverse square dependence holds, i.e.,

$$F(z) \approx k^2 w_0^2 / 4\pi z^2 \quad \text{for } z \gg z_0.$$

3. SENSITIVITY CALCULATION

In this section, we perform an initial sensitivity calculation for the lidar system. As seen in the previous section, these calculations rely on ascertaining a number of system parameters as well as atmospheric conditions including: atmospheric and optical transmissions, turbulence and aberration effects on the overlap function, target material reflectivity, and transmit as well as LO beam characteristics. We discuss our estimates of these parameters/effects in the following subsections. In the last part of this section, we compare the calculated sensitivity to measurements of target returns obtained during GABLE.

3.1 Beam Sizes and Overlaps

Given the TEA laser cavity length ($L \approx 96$ cm) and output coupler curvature ($R \approx 10$ m), the e^2 radius of the TEM₀₀ mode at its waist (the internal grating) can be found from:

$$\begin{aligned}w_G &= [\lambda(R/L-1)^{1/2}]^{1/2} \\ &= 3.2 \text{ mm.}\end{aligned}$$

In the present configuration, the distance along the TEA beam from the grating to the telescope secondary is about 3.8 m. Using equation 2.1.2a, we calculate the width of the TEA beam at the secondary to be 5.1 mm. This gives an expanded (25x) beam width (w_0) of about 5.0" and a Fresnel length (see equation 2.5.3) of 4.8 km. These results are sufficient to calculate the overlap function $F(z)$ versus range (from equation 2.5.2) for the ideal conditions discussed in section 2.5.

3.2 Optics Transmission

Table 3.2.1 and 3.2.2 list our estimates for the transmittance/reflectance of the transmitter/receiver optical components. The reflectance of the relay mirrors (Newport ER.2 coating) has been estimated from the manufacturers published typical performance curve. The reflectance of the SiO coated Al scanning and telescope

mirrors has been estimated from measurements made on similar mirrors [3.1]. (Note that a lower reflectance for the scanner mirrors is expected due to the 45° incident angle of the beam.) Typical manufacturer (II-VI, Inc.) specifications are assumed for the thin film polarizer (TFP), Rhomb, lens and beam splitter. We have been somewhat conservative in assuming a minimum of 2% insertion loss for these elements. We feel, however, that the results obtained for the transmitter and receiver transmissions are high due to expected environmental contamination of the scanner mirrors (and possibly the telescope primary).

TABLE 3.2.1 Transmitter Optics

Item Descr.	ref/trans	# of elements
relay mirror (ER.2)	0.98	4
tele. mirror (Al-SiO)	0.97	2
scan. mirror (Al-SiO)	0.95	3
TFP	0.95	1
Fresnel Rhomb	0.98	1
Total Transmission Throughput (T_T) = 0.69		

TABLE 3.2.2 Receiver Optics

Item Descr.	ref/trans	# of elements
scan. mirror (Al-SiO)	0.95	3
tele. mirror (Al-SiO)	0.97	2
Fresnel Rhomb	0.98	1
TFP	0.975	1
relay mirror (ER.2)	0.98	2
beam splitter	0.93	1
lens	0.98	1
window	0.98	1
Total Reception Throughput (T_R) = 0.66		

3.3 Atmospheric Transmission

For calibration as well as evaluation of system performance, it is necessary to correct for the atmospheric transmission from the LIDAR to the target. As the extinction of 10.6 μm radiation in the lower atmosphere (i.e., below the inversion layer) and under typical conditions is predominantly due to absorption by the water vapor continuum, the transmission is highly dependent on the relative humidity and to a lesser degree on the temperature. Therefore for accurate calibrated backscatter measurements it is necessary to characterize the atmospheric conditions and model or otherwise measure the transmission.

For the present purpose of preliminarily evaluating performance, we take conditions typical of those encountered on the GABLE field operation. Table 3.3.1 lists the results of PCTRAN (based on LOWTRAN6 [3.2]) calculations for the atmospheric transmission at 10.6 μm over a 1 km horizontal path as well over the round trip distance to the target employed on GABLE. We adopted the standard midlatitude summer (ms) atmosphere with the Maritime 23 km visibility aerosol model. The default values were taken for all the parameters except relative humidity. The range of RH in this table is representative of the low altitude radiosonde measurements made during GABLE. (Also included for comparison are the atmospheric transmissions for the P(20) transition wavelength of CO_2 from a listing by McClatchey and Selby [3.3] for tropical (trop) and midlatitude winter atmospheres.) We indicate by the asterisk the value for T_A^2 which will be used in sensitivity calculation below.

TABLE 3.3.1 Atmospheric Transmission at 10.6 μm

Model	Absorption Coef	T(1km)	T(6.8km)
PCTRAN ms: 85% RH	0.34 /km	0.71	0.097
PCTRAN ms: 90% RH	0.38 "	0.68	0.073 *
PCTRAN ms: 95% RH	0.42 "	0.66	0.059
REF 3.3 trop	0.61 "	0.54	0.016
mw	0.096 "	0.91	0.52

Low resolution models for atmospheric transmission (such as LOWTRAN) should be sufficient for this calculation as the dominant source of extinction is a continuum and not a band. However, we feel that a careful evaluation of the accuracy and range of validity for the available atmospheric models should be made in the future as well as the adoption and possible testing of a standard model.

3.4 Target Reflectivity

The target reflectivity, ρ^* as discussed in section 2.4, is by definition the fraction of incident light per steradian backscattered toward the receiver. It is dependent on the angle of incidence to the average target normal and polarization state of the beam as well as the polarization mode to which the receiver is sensitive. For the GL/OPA CO₂ lidar, the transmitted beam is circularly polarized (CP) and the receiver is sensitive to CP light of the opposite sense. (Note: the backscatter of CP light from Rayleigh and spherical Mie particles as well as specular reflection results in such a reversal in the light helicity.)

Due to its portability and durability, the target material adopted was blue polystyrene foam [3.4]. Unfortunately, the target material characterization that JPL supplied [3.5] is insufficient without further assumptions to determine ρ^* for a receiver sensitive to CP light. Basically, JPL measured the linearly polarized light (both s and p) backscattered from a target sample with CP light incident at 45° to the surface normal. The results are listed in table 3.4.1.

TABLE 3.4.1 Measured Target Material ρ^*

Incident Polarization	Detected Polarization	
	s(LP)	p(LP)
right (RCP)	2.59×10^{-2}	4.17×10^{-2}
left (LCP)	2.77×10^{-2}	4.45×10^{-2}
average	2.68×10^{-2}	4.31×10^{-2}

It is not clear why measurements were made with both RCP and LCP incident light. Only an unusual and highly structured material surface would show any difference. The 6.5% discrepancy indicated in the table is probably a better estimate of the imbalance in the JPL quarter-wave retarding optics than of any physically preferred sense. Strengthening this argument is the fact that the ratio of s to p reflectivities in table 3.4.1 for RCP incident light differs by only 0.2% from that for LCP incident light. We adopt for the following treatment the averages of the measured RCP and LCP reflectivities and refer to them for convenience as ρ_s^* and ρ_p^* .

The state of polarization of the backscattered light is unambiguously given by the Hermitian polarization density matrix ρ [3.6] (not to be confused with the reflectivity ρ^*):

$$\rho = \begin{bmatrix} \rho_{ss} & \rho_{sp} \\ \rho_{ps} & \rho_{pp} \end{bmatrix}$$

where $\rho_{ss} + \rho_{pp} = 1$ and $\rho_{sp} = (\rho_{ps})^*$. The fraction of light detected by a receiver sensitive to some pure polarization state is found from

$$(3.4.1) \quad P(\psi) = \psi \rho \psi^\dagger$$

where ψ is a two dimensional row vector (and ψ^\dagger --its adjoint--a column vector) which represents the polarization state. For example, we can choose to work in a basis such that the representations for the linear s and p polarization filterings are:

$$\begin{aligned} \psi_s &= [1, 0] \\ \psi_p &= [0, 1]. \end{aligned}$$

Then ρ_{ss} and ρ_{pp} (as the notation was chosen to indicate) are the fractions of light detected through s and p orientated LP filters and, for the light backscattered from the target, are given by:

$$\begin{aligned} \rho_{ss} &= \rho_s^* / (\rho_s^* + \rho_p^*) \\ \rho_{pp} &= \rho_p^* / (\rho_s^* + \rho_p^*). \end{aligned}$$

In this basis, the vector representation for a CP filter (with sense designated simply by \pm) is:

$$\psi_{\pm} = [1, \pm i]/(2)^{1/2}$$

and the fraction of light detected through such a filter can be obtained from equation 3.4.1:

$$\begin{aligned} P_{\pm} &= 0.5[1 \pm i(\rho_{ps} - \rho_{sp})] \\ &= 0.5[1 \pm 2 \gamma \eta \sin \phi] \end{aligned}$$

where we have defined

$$\begin{aligned} \rho_{sp} &\equiv \gamma \eta e^{i\phi} \\ \eta &\equiv (\rho_{ss} \rho_{pp})^{1/2}. \end{aligned}$$

The parameter γ is related to the degree of polarization of the light. If $\gamma=1$, then the determinant of the polarization density matrix is zero and the light is in a pure polarization state (generally elliptical). On the other hand, light described by a matrix with $\gamma=0$ is as "unpolarized" as it can be consistent with $\rho_{ss} \neq \rho_{pp}$. The angle ϕ describes the phase of the residual polarization, e.g., $\phi = \pm \pi/2$ for light which is elliptically polarized with \pm sense and with axes as defined by the s and p directions, and $\phi=0$ or π for LP light.

It is clear from this discussion that the measurements made by JPL--which tell us only ρ_{ss} and ρ_{pp} --are insufficient to fully characterize the polarization state of the backscattered radiation, i.e. there is no way to obtain γ and ϕ without making assumptions. We first make the physically reasonable assumption that the residual polarization of the backscattered light is elliptically polarized along the axes determined by the target orientation and with a sense opposite to that of the incident CP light. Any other possibility would require the target surface to have a preferred direction (other than its normal) and/or sense (i.e. left-handed vs right-handed). Given this assumption,

the fraction of detected light for a receiver sensitive to CP light of the opposite sense to the transmitter is

$$P = 0.5 [1 + 2 \gamma \eta]$$

and for the effective reflectivity ρ^*

$$\rho^* = P (\rho_s^* + \rho_p^*).$$

A further assumption is now needed for the value of γ where $\gamma=0$ for complete depolarization of the scattered light and $\gamma=1$ for no depolarizing effects. Here no present guide is available and we take $\gamma=0.5$. Under this assumption we obtain for the reflectivity appropriate for the polarization configuration of the lidar: $\rho^*=5.02 \times 10^{-2}$.

3.5 System Performance

For the preliminary evaluation of system performance we will compare the measured IF pulse energy due to backscatter from the target to that predicted by equation 2.4.6 and the above estimates of system and atmospheric characteristics. The latter, using equation 2.4.1, is given by

$$\begin{aligned} e_C &= 2R_L(\eta q/h\nu)^2 P_{LO} T_R T_T \lambda^2 \rho^* e_T T_A^2(z_T) F(z_T). \\ &= 4.7 \times 10^{-14} \text{ J} \end{aligned}$$

where we have collected the assumed quantities below in table 3.5.1.

For a comparison to measurement, we took the series of target return measurements AU210001-AU210012 taken on 8/21/90 during the GABLE field program. Each of these data runs consisted of averaging the results of 100 laser shots. Using methods to be discussed later in the section on electronics and calibration procedures, we obtained an average return IF pulse energy of 4.3×10^{-15} J for these measurements--about 10 times lower than the estimate above. Although a factor of 3-4 could within reason be accounted for by our overestimating the optics/atmospheric transmission, detector quantum efficiency, and target reflectivity, we have no doubt

that the major portion of this discrepancy is due to the overestimate of the overlap function $F(z)$ which resulted from our assumption of idealized conditions. In particular, what must be accounted for and/or corrected is: the match of LO and TEA laser beam shapes; aberration and possible vignetting of the transmitted and virtual LO beam by the telescope and scanner mirrors as well as by atmospheric turbulence.

TABLE 3.5.1 Target Return Sensitivity Parameters

load resistance (R_L)	50 Ω
quantum efficiency (η)	0.5
LO power (P_{LO})	140 μW
receiver transmission (T_R)	0.66
transmitter transmission (T_T)	0.69
reflectivity (ρ^*)	5.02×10^{-2}
laser pulse energy (e_T)	75 mJ
atmospheric transmission ($T_A^2(z_T)$)	7.3×10^{-2}
overlap ($F(z_T)$)	13.1 m^{-2}

4. CO₂ LASER AND TRANSCEIVER OPTICS

Figure 4.1 illustrates the optical layout of the lidar. The labeled components are identified below in table 4.1. The lidar is constructed on two levels with the telescope and transmit/receive (T/R or lower) deck suspended from the laser (or upper) deck. The circles in the figure about mirrors M10 and M12 indicate the position of 2" diameter holes through the optical table which allow transfer of the TEA laser transmit pulses and the local oscillator (LO) beam to the lower deck. The position of these laser ports as well as mounting screw holes for the laser are shown more exactly in figure 4.2. Not shown in the diagram is a large turning mirror which directs the emergent beam vertically into a hemispherical scanner.

Table 4.1
Optical Components

M1-2	beam steering assemblies
M3-20	mirrors
B1-4	beam splitter/combiners
IR1-4	irises
BX	4x beam expander
VA	variable attenuator
FA	fixed attenuator
CH	chopper
AOM	acousto-optical frequency shifter
W1-2	intra-cavity Brewster windows
G	TEA laser grating
OC	TEA laser output coupler
L1	lens
TFP	thin film polarizer
RH	Fresnel quarter wave rhomb
DET	cryogenic HgCdTe detectors

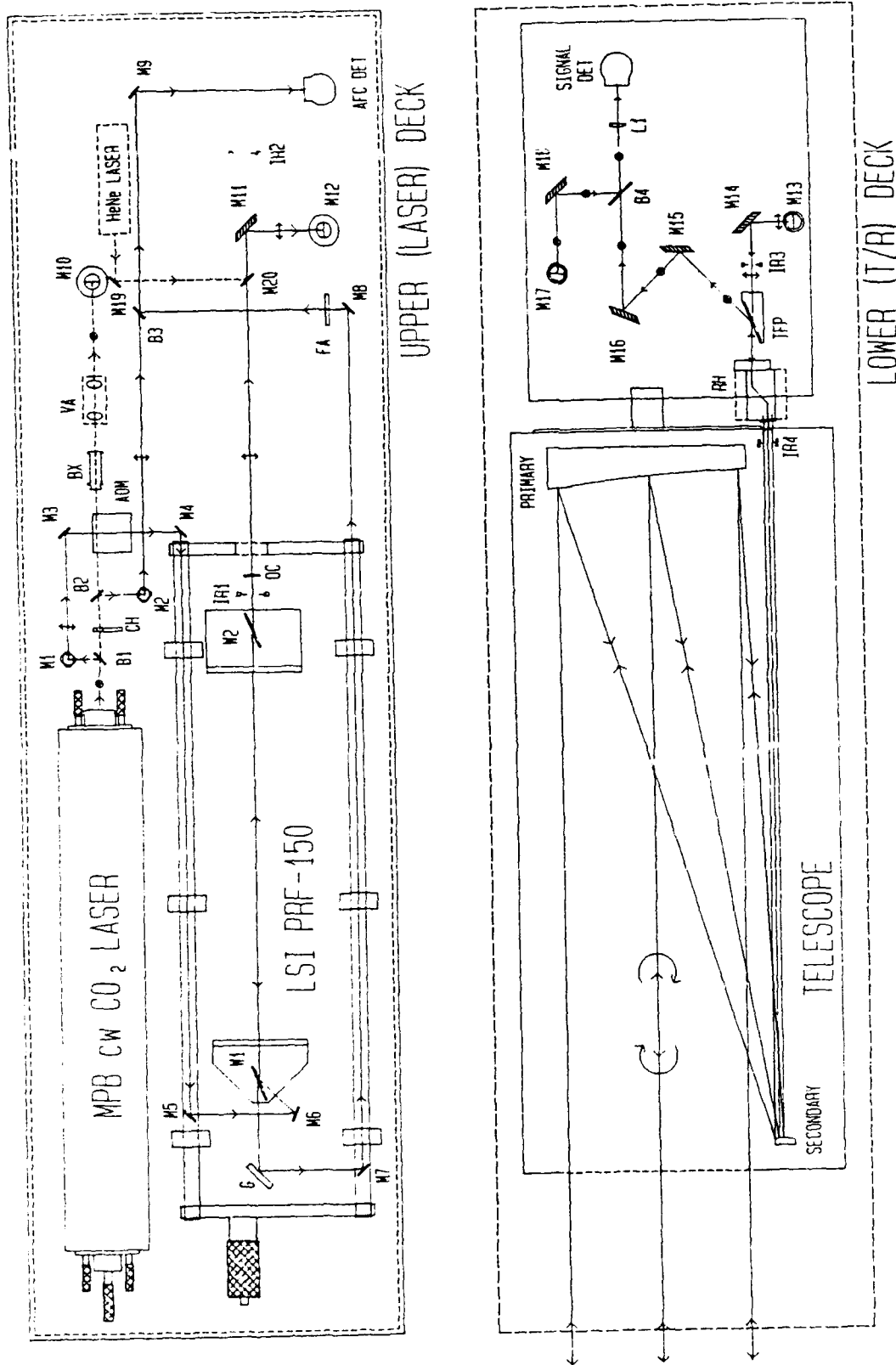


Figure 4.1 Schematic of Transmitter/Receiver Optics.

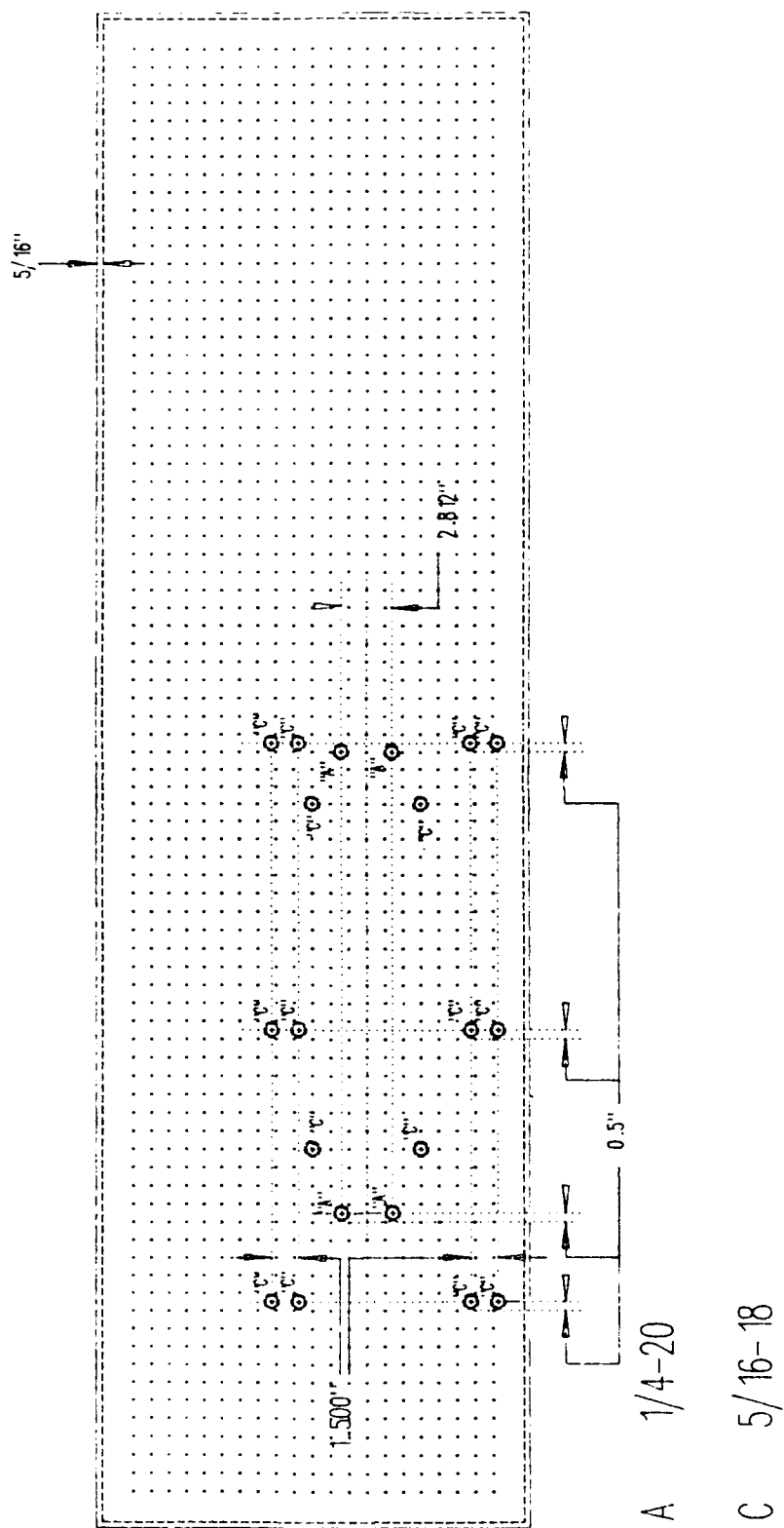


Figure 4.2 Optical Table Modifications.

The TEA laser itself is an LSI PRF-150 which was modified by LSI for injection-locked operation. Additional modifications were made to some laser component mounts, the injection and AFC pickoff scheme, and the cw beam steering optics. These changes were made to: allow for installation on a 2'x7' optical table; reduce the transmission of vibrations from the laser head fans to the cavity optical components; allow for the use of a vertically polarized cw laser; and to eliminate the necessity for a beam splitter in the TEA laser beam.

4.1 Initial Laser Alignments

4.1.1 CW Laser

Procedures for the internal alignment and operation of the cw laser are given in the MPB manual. We discuss below procedures for initial installation and alignment of the derived beams.

The working height on the upper deck is 3.125" and on the lower deck 4.875". The exception to this is the cw beam which emerges from the MPB laser vertically polarized and at a table height of 5.25". This beam is indicated by a dashed line in figure 4.1. The portions of this beam picked off by the beamsplitters B1 (the seed for injection locking) and B2 (the LO for the AFC detector) are displaced to the upper deck working height by the assemblies M1-2. Due to the configuration of these assemblies, the polarization of these deflected beams is horizontal. There is no beam steering element for the portion of the cw beam which traverses the beam splitter (the signal LO). Because of this, it is important that during installation of the cw laser on the optical bench the output beam be checked to ensure that it passes over the center of the laser port at M10. When this is done the mount for M10 should be adjusted vertically so that the signal LO beam strikes the center of M10 and is deflected down through the laser port. Further alignment of this beam to the signal detector will be discussed later in the section on the T/R optical alignment.

For initial alignment of the seed beam, mirrors M1 and M3 should be adjusted so that this beam passes through the center of the AOM and strikes near the center of M4. Then with the power (and cooling water) to the AOM turned on, the AOM mount should be rotated until a deflected emerging beam is seen. This indicates that insertion

is at the correct Bragg angle for a frequency shift of 40 MHz. Fine adjustments of the AOM angle will maximize the power in the shifted component. The location of the beam on M4 should be checked again. Due to the deflection by the AOM, it may no longer be near the center of the mirror. The above process should be iterated until the shifted seed beam can be deflected by M4 to M5.

For the AFC/LO, mirrors M2 and M9 should be adjusted to direct this beam through the center of the beamsplitter B3 and to the center of the AFC detector's entrance window. This should be done with the AFC detector cooled and blocked. Then with the chopper (CH) turned on and the detector unblocked, adjust M9 to maximize the chopped detector current. This will ensure that the AFC/LO is centered on the detector. (A discussion of detector and biasing operation and procedures is given in a later section on the receiver electronics.)

4.1.2 TEA Laser

Procedures for the internal alignment and operation of the TEA laser are given in the LSI manual. (Injection locked operation is not contained in the LSI manual and will be discussed in the next section.) A number of checks and alignments with the laser firing are suggested to simplify the seed and AFC pickoff alignments discussed in the next section. First check that the output from the laser is exiting through the center of the output coupler (OC). If the beam is significantly off center, correct it by "walking" the laser axis using the grating and output coupler tilt controls. Also check that the (low energy) zero order reflection off the grating is on the same vertical level as the center of mirror M7 and position this mirror to intercept this "pickoff" and direct it towards M8.

When the laser operation is considered satisfactory, a HeNe laser beam is aligned with the cavity. To do this remove M20 and M11 (which are kinematically mounted to allow for precise replacement) and, with the laser firing, center the iris IR2 on the TEA laser beam. (We have also found it useful for the T/R alignment to allow the beam to propagate several feet past IR2--as much as is possible--and strike/mark a fixed target of thermal paper.) With the TEA laser turned off, place a temporary mirror in line with the TEA laser and on the far side of IR2 (e.g., near the table edge) and direct the HeNe beam at this mirror by rotating M19. Using the tilt controls for this temporary mirror, M19, and/or the HeNe laser mount, walk the HeNe beam until

it passes through the center of the iris (IR2) and the output coupler. A number of reflections (probably three) off the output coupler should now be observable. This series of reflections is due to the wedge of the output coupler. The middle (or second brightest) reflection is due to reflection off the inner surface. Continue to walk the HeNe beam until both it and this reflection pass through the center of IR2. When this is done, it should be possible to trace the reflection all the way back to the exit aperture of the HeNe laser. The HeNe beam is now lined up with the TEA laser cavity axis.

4.2 Injection Locking: Seed and AFC Alignment

4.2.1 Seed Beam Alignment

The seed laser is to be injected into the cavity by reflection off the Brewster window W1. With the HeNe laser aligned as discussed above, a dim though visible amount of HeNe light should be observable exiting the side window on the mount for W1. Position M6 to intercept this beam and then adjust the tilt of M6 and M4 so that the HeNe beam and the seed beam overlap at the surface of M5. Then adjust the tilt of M5 so that the HeNe strikes the center of the exit aperture of the AOM. The seed beam should now be aligned with the cavity axis.

4.2.2 AFC Pickoff Alignment

With the HeNe laser aligned as above, multiple diffracted beams should be observable from the TEA grating. A single dim order (the zeroth) should be striking M7 if this mirror was positioned as discussed in section 4.1.2. With the fixed attenuator FA removed and the cw laser on, adjust M7 and M8 so that this beam overlaps the AFC/LO at the surface of B3. Then adjust the tilt of B3 to overlap these beams at the surface of M9. This last step is difficult due to the low brightness of the HeNe light reflected off B3 and must be executed with all room lights off. After this step is complete replace the fixed attenuator and insert a stop in front of IR2 to prevent the TEA laser from striking the iris.

4.2.3 Injection Locked Operation

When the above alignments are complete and with the AFC detector cooled, attach the detector output to the NERC amplifier and the output of the amplifier to both

the pulse frequency counter (PFC) and an oscilloscope. Turn on the amplifier, PFC, and the EMT driver with the latter in closed loop/unlocked mode. Turn on the TEA laser. With the AFC/LO blocked, a detector pulse on the order of several hundred millivolts should be observed. Fine adjustment of the alignment of the TEA laser pickoff can now be done by utilizing M8 and B3 while observing the detected pulse. When the AFC/LO is unblocked, beating between the LO and the TEA pulse should be observable with the frequency of this beat varying as the position of the output coupler is manually changed with the EMT driver. As the output coupler is slowly scanned, a position will be reached where the AFC signal waveform dramatically changes: the beat frequency will stabilize at 40 MHz and the laser firing time will advance by 100-200 nsec and exhibit reduced jitter. At this cavity length, the frequency of the TEM₀₀ mode of the TEA laser is matched to that of the injected seed radiation and the output is injection locked. The PFC counter should indicate 40 MHz with pulse-to-pulse jitter less than about 1 MHz. Switch the EMT driver to open loop/locked mode. This will compensate for thermal cavity length drifts and low frequency vibrations.

4.3 Transmit/Receive Optical Alignment

4.3.1 Initial HeNe Alignment

With mirror M11 removed, insert M20 and use this along with M19 and/or the HeNe laser mount to line the HeNe beam with the center of IR2 and the spot made on the fixed target in section 4.1.2. This lines the HeNe beam up with the TEA laser beam. Replace M11 and position it so that the HeNe spot is centered on the mirror. Now use M11, M12, M13, and M14 to pass the HeNe beam through the center of the TFP, Fresnel rhomb, and iris IR4. This will require a number of iterations to correctly position the TFP and rhomb. When this is finished observe where the HeNe beam strikes near the secondary. Using M12 and M14, walk the beam until it passes through the center of IR4 and strikes near the center of the secondary mirror. It is difficult to judge this centering on the secondary so that for fine adjustments the position of the expanded spot on the primary should be checked. Now center the iris IR3 on the HeNe beam. This allows the two irises IR3-4 to be used for future alignments to the telescope optic axis.

A temporary mirror is mounted inside the telescope side access panel which can be swung down to intercept the beam several inches past IR4. Insert this mirror and adjust it to retroreflect the HeNe beam back through the irises. With a good alignment this retroreflected beam can be traced all the way back to the HeNe laser exit aperture. A second beam reflected by the TFP towards M15 should be observable. Use the position and tilts of M15 and M16 to direct this beam through the center of the beam splitter B4 and the lens L1.

4.3.2 LO Alignment

With the signal detector removed and the attenuator VA set for 100% throughput, use mirrors M10, M17, and M18 to deflect the LO through the center of B4. By placing a thermal card out past B4 towards the rear of M14, both the LO which is transmitted through B4 (95%) and that portion of the HeNe beam which is reflected by B4 should be observed. These should be coincident along the 6-7" path length observable. For coarse adjustment use M17 and M18 to redirect the LO. For fine adjustments, use the tilt control for B4. When this is done, check the alignment by placing a thermal card at the detector position. The focused HeNe and LO spots should be observed to be coincident.

To align the detector, turn the attenuator down to a setting of about 10, cool and replace the detector, and turn the chopper on. Then adjust the detector and lens position (including focus) to maximize the chopped detector current. (A discussion of detector and biasing operation and procedures is given in a later section on the receiver electronics.)

At this stage the LO is lined up with the detector but the receive optics can only be considered to be coarsely aligned to the telescope axis. We use the fraction of the seed laser which is transmitted by the TEA cavity for the final alignment. To do this, remove M20. Now the weak transmitted seed beam traverses the transmit optics and is retroreflected to the detector by the mirror after IR4. To observe the signal produced by the seed, connect the output of the detector to the signal 30 dB preamplifier and the amplifier output to an oscilloscope. A 40 MHz signal should be observed due to the beating between the seed and the LO. Moreover, the amplitude of this signal should vary as the TEA cavity length is changed by manually controlling the EMT driver. The TEA laser cavity is effectively operating as an etalon. With the EMT set to

produce the largest beat signal, mirrors M15 and M16 should be adjusted to maximize the signal.

When this stage is reached, the incident LO power on the detector should be slowly increased by raising the setting of the attenuator VA. As this is done, the beat signal level will be observed to slowly increase up to a point and then rapidly decrease thereafter. The reasons for this will be discussed in a later section on receiver electronics. In principle the attenuator should be set for maximum signal; however, to ensure against small upward cw laser power drifts it is preferable to choose an LO power slightly smaller than that which delivers maximum signal.

4.3.3 Final T/R Alignment

Due to the difficulty in achieving near perfect alignment between the TEA and the HeNe beams (4.3.1), we have found it necessary to perform a final iteration of some of the above procedures to ensure that the transmit and receive axes are aligned well. First with the mirror past IR4 removed and the signal detector blocked, the TEA laser is turned on and its alignment to irises IR3-4 observed. In addition a handheld detector can be used to find the center of the expanded beam at the output end of the telescope. If the result of the observations is that the TEA beam is aligned with the telescope axis, then the alignment of the lidar is finished. If, on the other hand, small displacements are noted, then mirrors M14 and M12 are used to correct these. This adjustment effects the pointing of the seed beam which was used for the receive axis alignments. Therefore the final stages of 4.3.2 must be repeated. Notably, with the TEA laser turned off and M20 replaced, mirrors M20 and M19 along with the HeNe laser mount are adjusted to line the HeNe beam up with the centers of IR3 and IR4. The temporary mirror is then inserted on the far side of IR4 and adjusted for retroflection. M20 is then removed and the beat signal is maximized as above. Removal of the retro mirror completes the alignment procedure.

5. RECEIVER ELECTRONICS

5.1 Detector and Bias Circuitry

The detectors employed for both the signal reception and AFC systems are NERC HgCdTe liquid N₂ cooled photovoltaic diodes. At 10.6 microns, the quantum efficiency of these detectors is about 50% with response on the order of 4 A/W, a signal bandwidth on the order of 100 MHz when reversed biased, and detector noise very nearly Johnson noise limited. Figure 5.1.1 shows the typical biasing scheme for these detectors. In this figure standard use of upper case letters to denote the dc values of current and voltage is employed. R_p and C_p are the diode junction shunt resistance and capacitance. The representation of the detector operation by idealized components is only approximate. In practice there is a significant degree of non-linearity in the diode IV curve and R_p is usually taken to correspond to the differential resistance at zero bias. Moreover, the junction capacitance decreases and the detector bandwidth increases as the reverse bias voltage increases. This results from the increase in the width of the junction depletion layer with reverse bias.

For the idealized detector illustrated in figure 5.1.1, the junction voltage is given by

$$V_0 = (V_B - R_B I_{LO}) / (1 + R_B / R_p),$$

where

V_B ≡ bias supply voltage,

R_B ≡ bias resistance,

I_{LO} ≡ dc photocurrent induced by the LO (= response x P_{LO}).

With no LO radiation incident, the junction voltage is determined by the current (I_p) flowing through the diode shunt resistance. As the intensity of the LO is increased, the junction current increases which reduces the amount of bias current passing

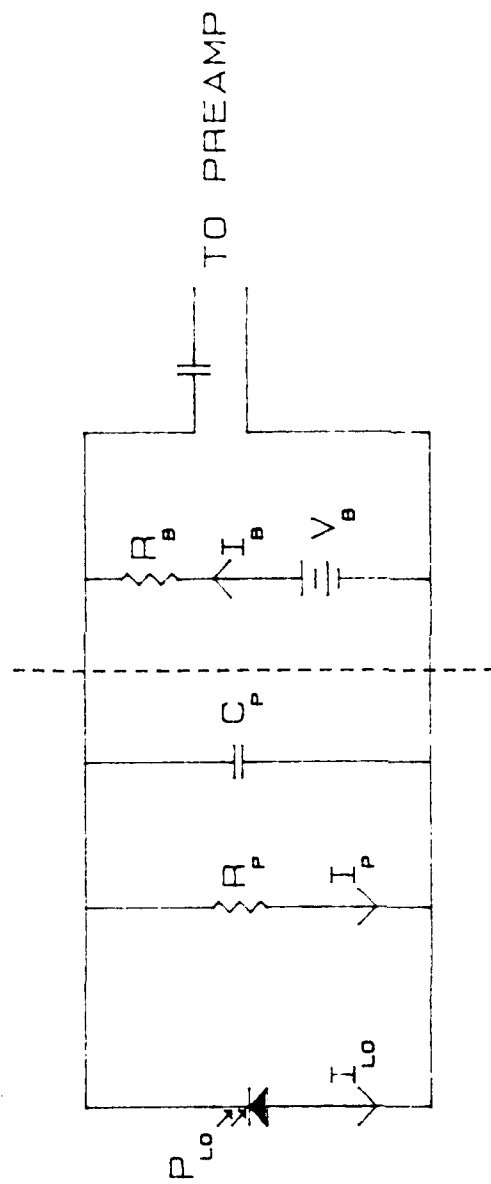


Figure 5.1.1 Bias Scheme for HgCdTe Detectors.

through the shunt resistance and thereby reduces the junction voltage. When $I_{LO} = V_B/R_B$, the junction voltage is zero and there is no reverse bias. This explains the behavior discussed in section 4.3.2. As the LO field increases, the IF signal first increases as expected and then dramatically falls off. This decrease is due to the increase in junction capacitance (and resultant decrease in detector bandwidth) as the reverse bias approaches zero. This effect provides a limit in addition to the damage threshold for the amount of LO which can be employed since the manufacturer suggests an upper limit of about 1 mA for the bias current. In the next section, we discuss the implications of this on obtainable signal to noise levels.

To check the operation of the detectors under different bias conditions and to measure the chopped signals used to align the AFC and signal LO to the detectors, we constructed a bias test box. The schematic for this circuit is shown in figure 5.1.2. This box allows for a selection of a wide range of bias resistances. As discussed in the next section, typical operation from a 9 V supply is with a 9 k Ω bias resistance (i.e., a maximum bias current less than about 1 mA). Figure 5.1.3 shows the use of this circuit to monitor the chopped LO signals employed to align the AFC and receiver LO beams (as discussed in section 4.1.1).

5.2 Detector/Preamp Circuits

For the analysis of detector/preamplifier noise, the simple model illustrated in figure 5.2.1 is used. We adopt for the sake of example the specifications of detector S-10. From the NERC test report these are:

output impedance (R_p)	300 Ω
responsivity	4.8 A/W.

The amplifier employed is an Anzac AM-113 with the following specifications:

gain	30 dB
noise figure	2 dB
input impedance	50 Ω .

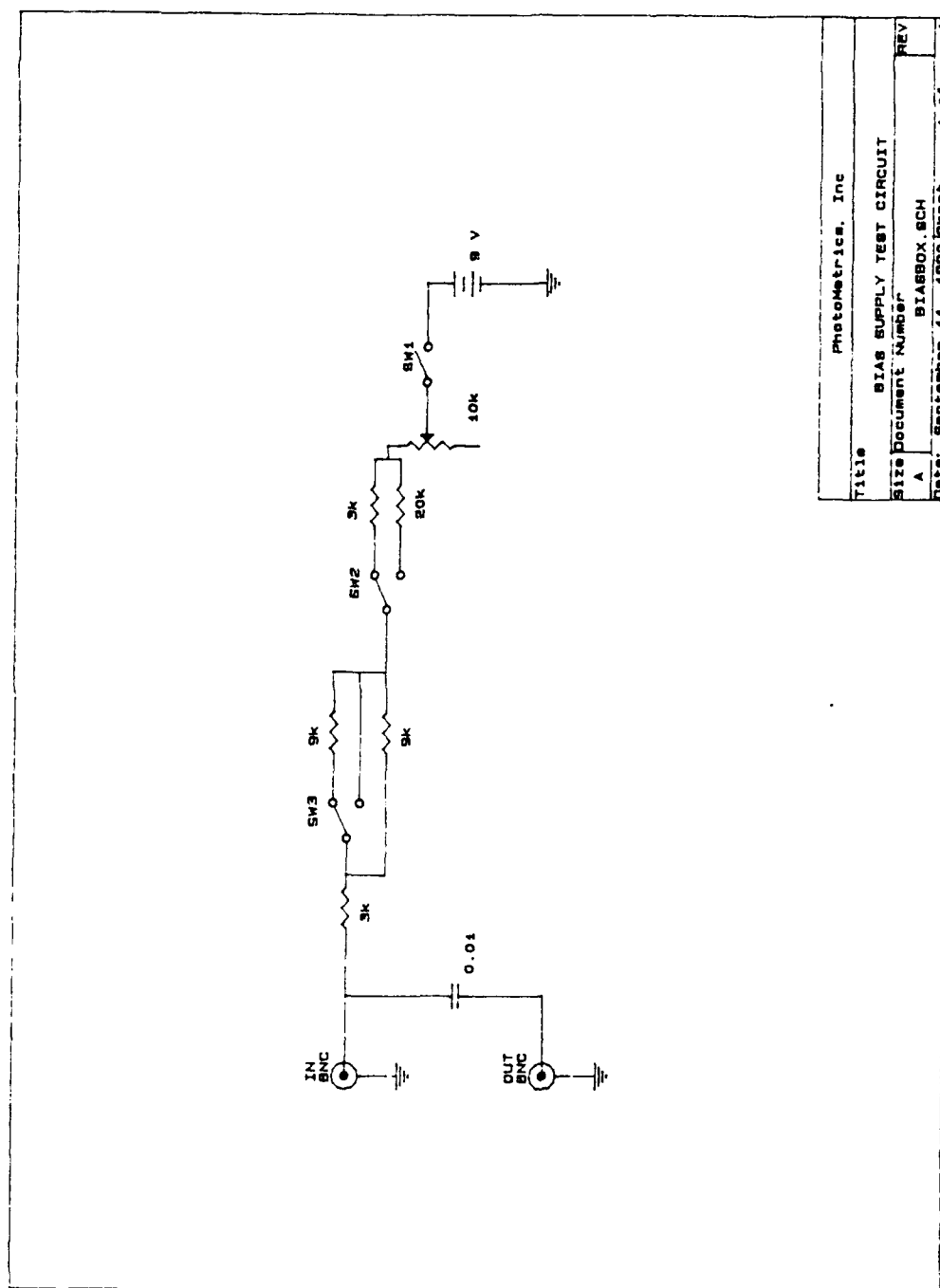


Figure 5.1.2 Schematic of bias test circuit.

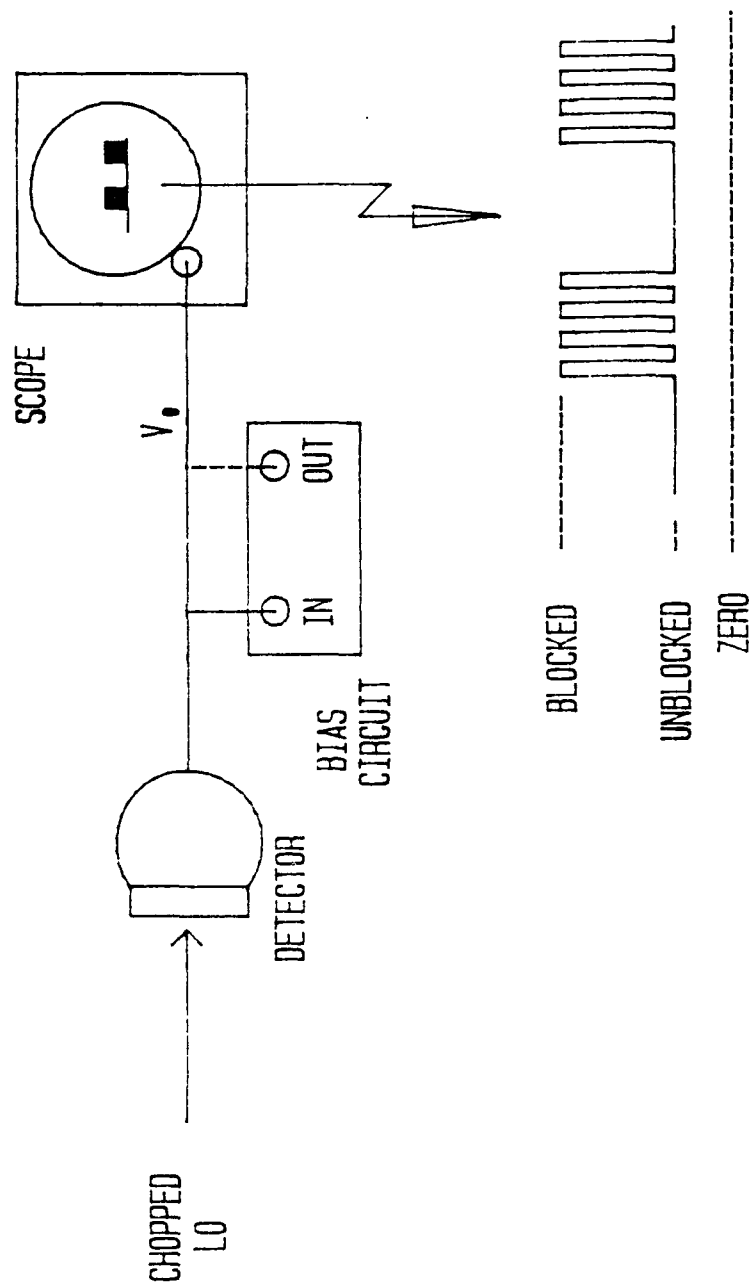


Figure 5.1.1.3 Illustration of the use of the bias test circuit to monitor chopped CW signals.

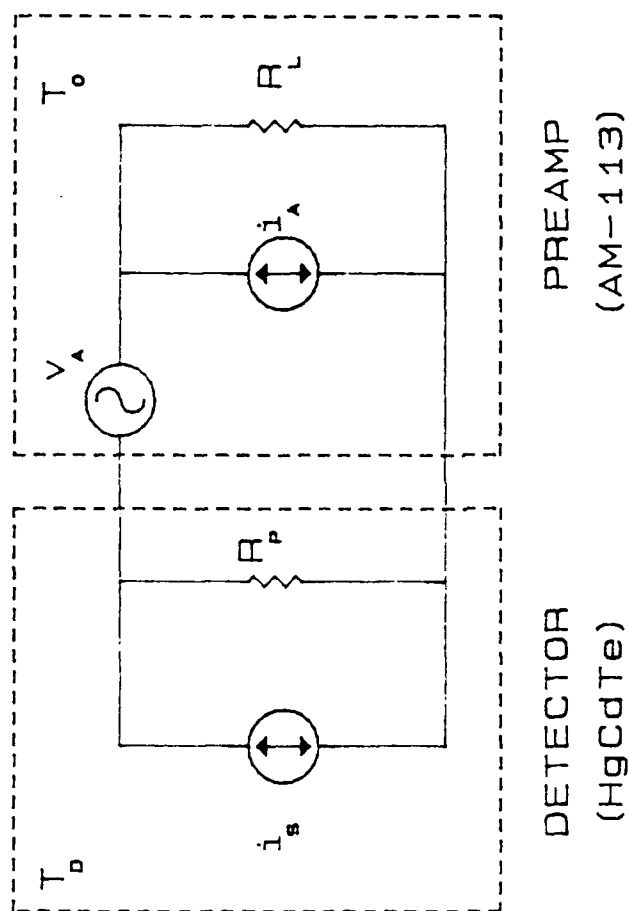


Figure 5.2.1 Detector/Preamplifier Noise model.

The detector noise current has both a thermal and a nonthermal--bias voltage dependent--component. The rms Johnson noise current per unit bandwidth for a detector temperature (T_D) of 77° is

$$i_D = 4kT_D/R_P = 3.8 \text{ pA}/\sqrt{\text{Hz}}.$$

As the nonthermal noise current in similar detectors has been reported to be less than this, we will take the above as an estimate of the total noise current. The quantities i_A and v_A are current and voltage noise source models for the preamplifier added noise. The matched source noise factor, F , is related to these by [5.1]:

$$(v_A)^2/R_L + R_L(i_A)^2 = 4kT_0(F-1)$$

where T_0 is the laboratory temperature and R_L is the amplifier input impedance.

For the AM-113 (and for most similar IF amplifiers), the relative magnitudes of v_A and i_A are not specified as only matched source usage is envisioned. We consider the three cases where: (i) the added voltage noise dominates ($v_A \gg R_P i_A$); (ii) the added current noise dominates ($i_A \gg v_A/R_A$); and (iii) matched conditions apply. Under these conditions the effective total noise power delivered to the load can be found from figure 5.2.1 to be:

$$\begin{aligned} \text{case i} \quad N_L &= 4kR_L [R_P T_D + R_L T_0(F-1)]/(R_L + R_P)^2 \\ &(7.2 \times 10^{-22} \text{ W}/\sqrt{\text{Hz}}), \end{aligned}$$

$$\begin{aligned} \text{case ii} \quad N_L &= 4kR_L [R_P T_D + R_P^2 T_0(F-1)/R_L]/(R_L + R_P)^2 \\ &(7.6 \times 10^{-21} \text{ W}/\sqrt{\text{Hz}}), \end{aligned}$$

$$\begin{aligned} \text{case iii} \quad N_L &= k [T_D + T_0(F-1)] \\ &(3.5 \times 10^{-21} \text{ W}/\sqrt{\text{Hz}}). \end{aligned}$$

In the following discussion, we adopt the largest of these estimates (case ii).

To obtain the largest possible signal to noise ratio the detector should be operated in the regime where the shot noise due to the LO is greater than or equal to

the detector and added preamplifier noise. The mean square shot noise current per unit bandwidth is given by

$$i_{SH}^2 = 2 q I_{LO}$$

where q is the electron charge and I_{LO} as above is the LO induced dc photocurrent. The mean square detector noise current which would deliver N_L to the preamplifier is

$$i_N^2 = (R_P + R_L)^2 N_L / R_L R_P^2 = 2.2 \times 10^{-22} \text{ A}^2/\text{Hz}.$$

For the shot noise to dominate the detector/amplifier noise: $i_{SH} \geq i_N$, and solving for I_{LO} :

$$I_{LO} \geq i_N^2 / 2q = 0.68 \text{ mA}.$$

This requires the LO incident power to be greater than about 0.14 mW.

The operating condition of the signal detector was investigated under conditions afforded by the manufacturer's suggested maximum bias current (1 mA). With a bias supply voltage (V_B) of about 9 V and a bias resistance of about 9 k Ω , the LO power was slowly increased until a maximum was observed in a 40 MHz beat signal. For this detector, this occurs at a junction voltage (V_0) of about 280 mV. The bias resistance current (I_B) at this setting was measured (0.99 mA). Then the local oscillator was blocked and the bias resistance increased until the same junction voltage was obtained. The bias current under these conditions was measured to be 0.25 mA. As the bias and signal current are related by:

$$I_B = I_{LO} + I_P(V_0),$$

the difference between these currents is the signal current induced by the LO. Thus under these bias conditions the maximum obtainable signal current is 0.74 mA corresponding to an incident power of about 0.15 mW. From the above discussion of expected noise levels, these results indicate that detection at or near the shot noise limit is possible under these conditions. Indeed qualitative comparisons of the noise levels

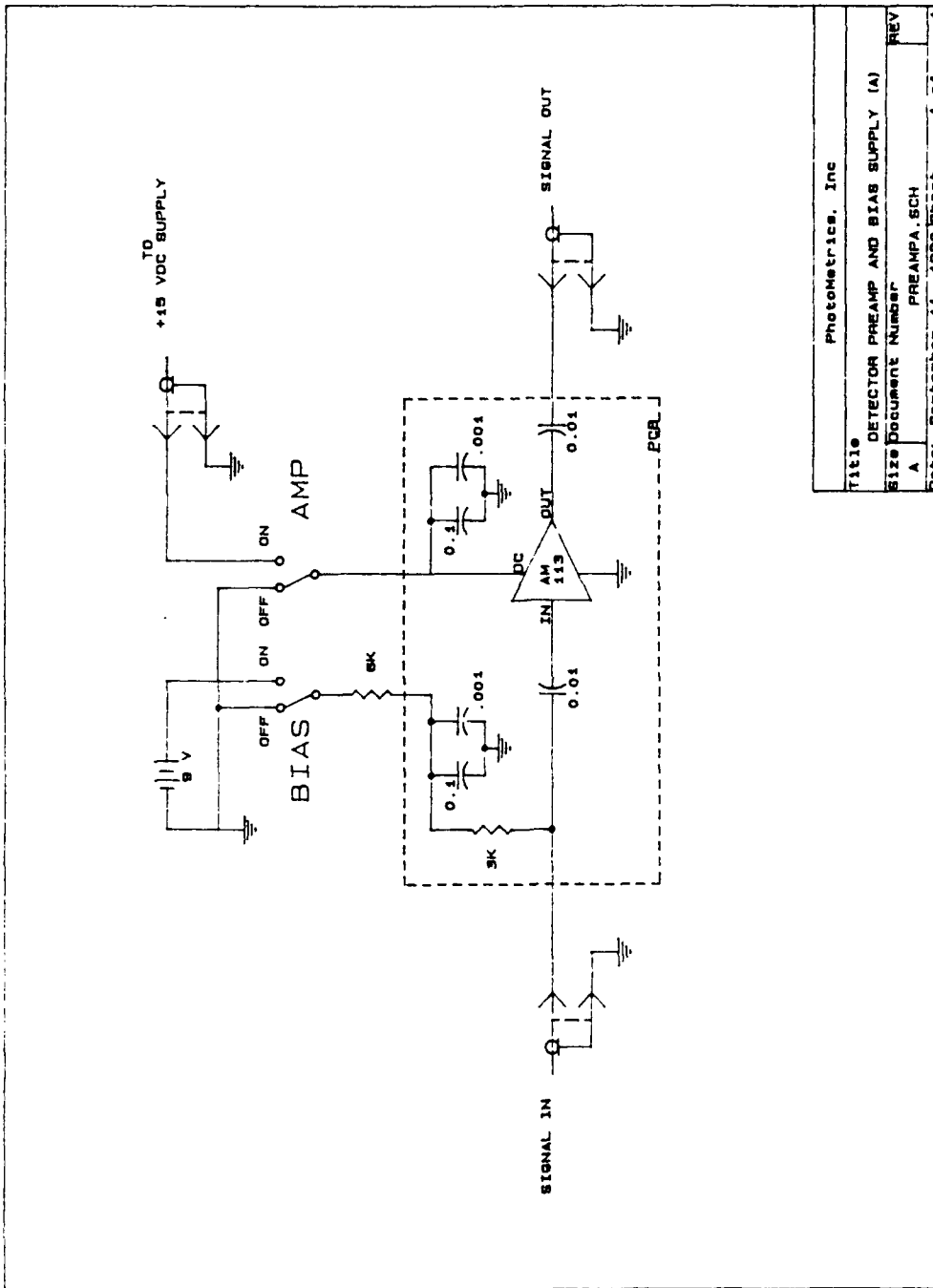
observed with and without the LO indicated an increase by about a factor two in noise power. Note that for such a comparison to be valid, the noise measurement with an incident LO beam should be compared to the noise observed without incident radiation and the bias voltage supply or resistance altered to produce the same junction voltage. This will ensure that the same differential source impedance and capacitance apply in the two cases. Future evaluations of the detection system should include quantitative measurements of the obtainable noise levels as well as investigations of the NERC detector limitations and those for HgCdTe detectors available from other sources. A recent study [5.2] indicates a lower than expected heterodyne quantum efficiency from similar detectors. This may be related to bandwidth considerations.

Figure 5.2.2a shows the schematic for the preamplifier/bias circuit constructed for the signal detection system. In keeping with the above considerations, it will supply about 1 mA of bias current. Figure 5.2.2b shows the schematic for a similar preamplifier/bias circuit constructed earlier and along lines suggested by GE [5.1]. Note that in this module, the bias current is limited to a value less than about 0.5 mA and according to the above discussion will not be capable of producing shot noise limited operation. This module can be easily modified to deliver a higher bias current and serve as a spare.

5.3 High Gain Amplifier and IF Electronics

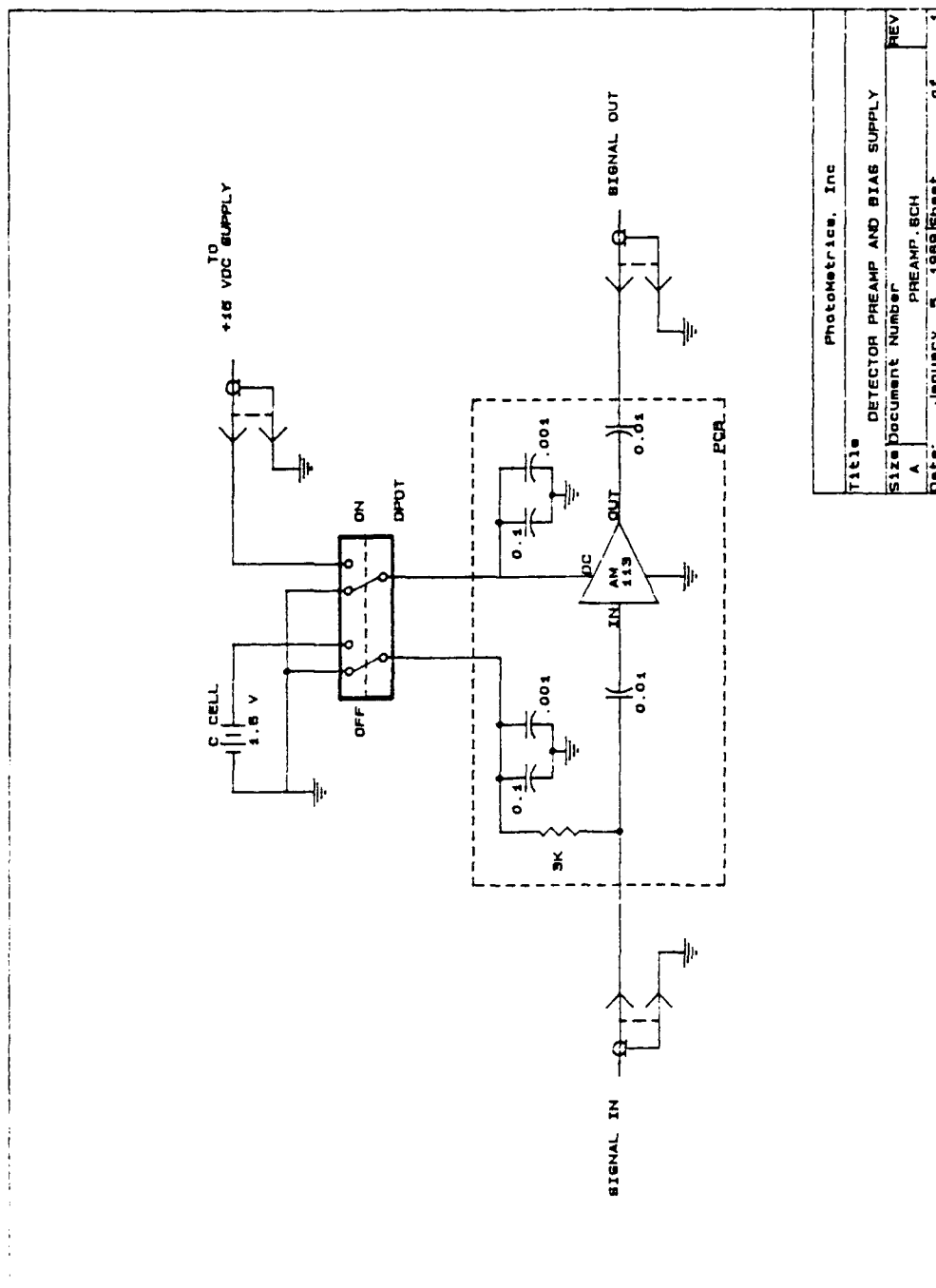
Figures 5.3.1a-f are the schematics for the IF amplifier unit which we constructed for the receiver. This unit contains two separate channels: a low ($\leq 25\text{dB}$) and a high ($\leq 70\text{ dB}$) variable gain amplifier. A block diagram of the rf module layout is shown in figure 5.3.1b. A complete list of the rf modules in the unit (as shown in figure 5.3.1b) is given in table 5.3.1 with manufacturer specifications in Appendix A. These modules are all connectorized so that rerouting and substitution is straightforward.

We have included in this unit for future possible use the log amplifier and frequency discrimination modules which were delivered to GL/OPA by GE;



Photometrics, Inc.		
Title		
DETECTOR PREAMP AND BIAS SUPPLY (A)		
Size Document Number		
A	PREAMPA.SCH	REV
Date: September 11, 1990	Sheet	1 of 1

Figure 5.2.2a Schematic of Preamp/Bias circuit ($I_B \approx 1\text{mA}$).



Photometrics, Inc.	
Title	DETECTOR PREAMP AND BIAS SUPPLY
Size	Document Number
A	PREAMP.BCH
Date:	January 5, 1988
Sheet	1 of 1

Figure 5.2.2b Schematic of Preamp/Bias circuit ($I_B \approx 0.5\text{mA}$).

however, these have not been used or tested beyond a preliminary check of their operability. Moreover, in all operations to date, the signal split-offs to these units (the power dividers M12 and M7) have been bypassed to avoid any possible interference. We do not discuss these units or their capability in this report.

Table 5.3.1
RF Module List

Module	Make	Model	Description
M1	MiniCircuits	ZFSWA-2-46	GaAs SPDT Switch
M2	EMF	EMF-5006	110 MHz Oscillator
M3	ANZAC	MD-140	Mixer
M4,12	ANZAC	THV-50	Power Divider
M5	K&L μ Wave	6LB31-70/5	70 MHz Filter, 5 MHz BW
		6LB31-70/10	70 MHz Filter, 10 MHz BW
M6	RHG	LST60E13FP	70 MHz Log Amplifier (13 MHz BW)
M7	K&L μ Wave	4LL32-90/150	Low Pass Filter, 90 MHz cutoff
M8	RHG	DT7020C	70 MHz Limiter/Discriminator
M9	RHG	ICEVT7030C	Linear 70 MHz Amplifier (30 MHz BW)
M11	RHG	ICF40E13FN	Linear 40 MHz Amplifier (13 MHz BW)
M13	RHG	DT40E13FN	40 MHz Limiter/Discriminator

We have found the low gain amplifier useful for utility purposes and as a spare heterodyne signal preamplifier when used with the bias test box. Its 13 MHz bandpass (± 6.5 MHz) about the heterodyne IF frequency (40 MHz) may make this amplifier useful for suppressing out of band transients in the AFC loop; in addition, its gain control would supply the capability for varying the AFC signal level to the PFC. The gain of this amplifier is manually adjustable with the front panel knob labeled R9 in figure 5.3.1c.

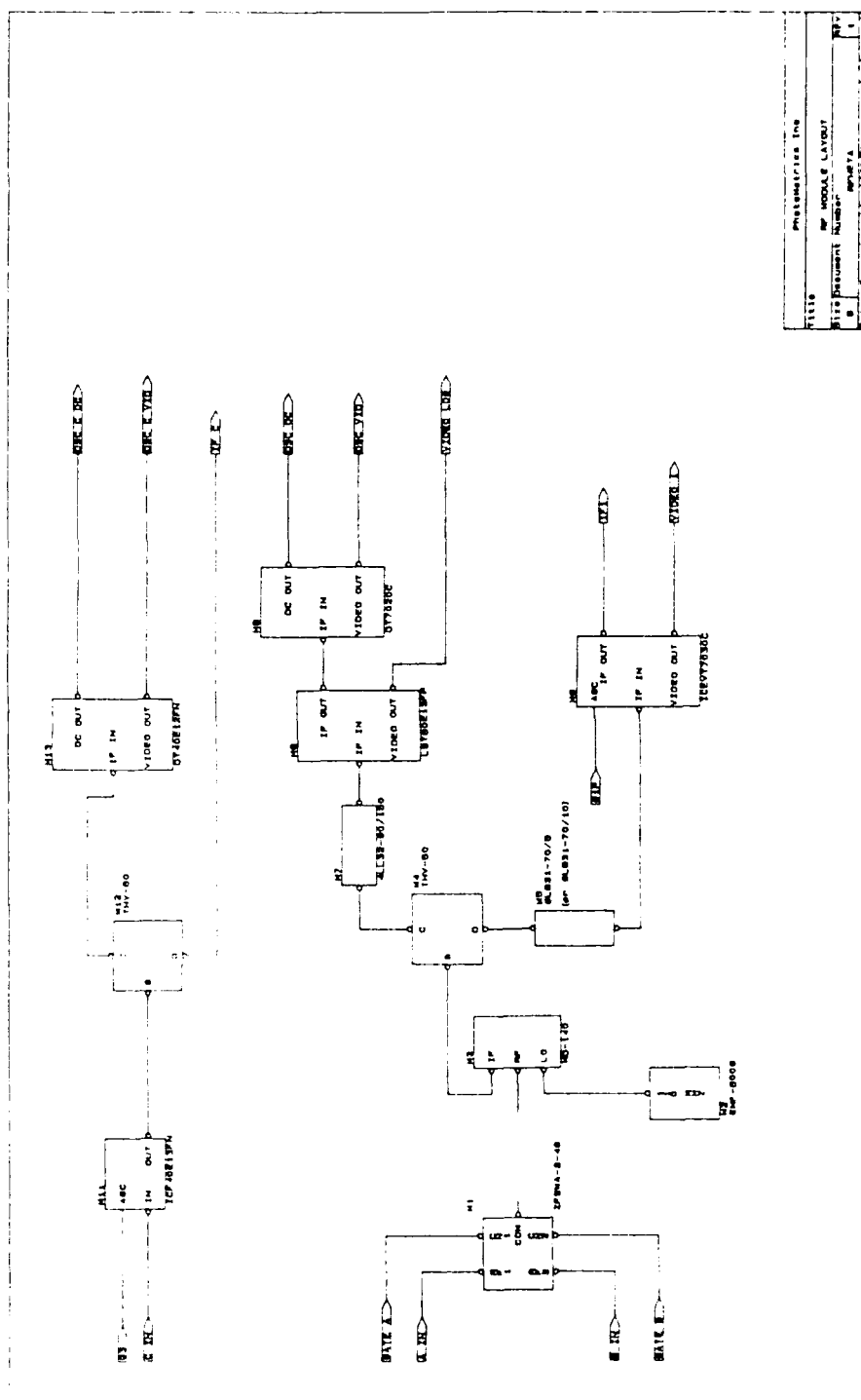


Figure 5.3.1b Amplifier unit: RF module layout.

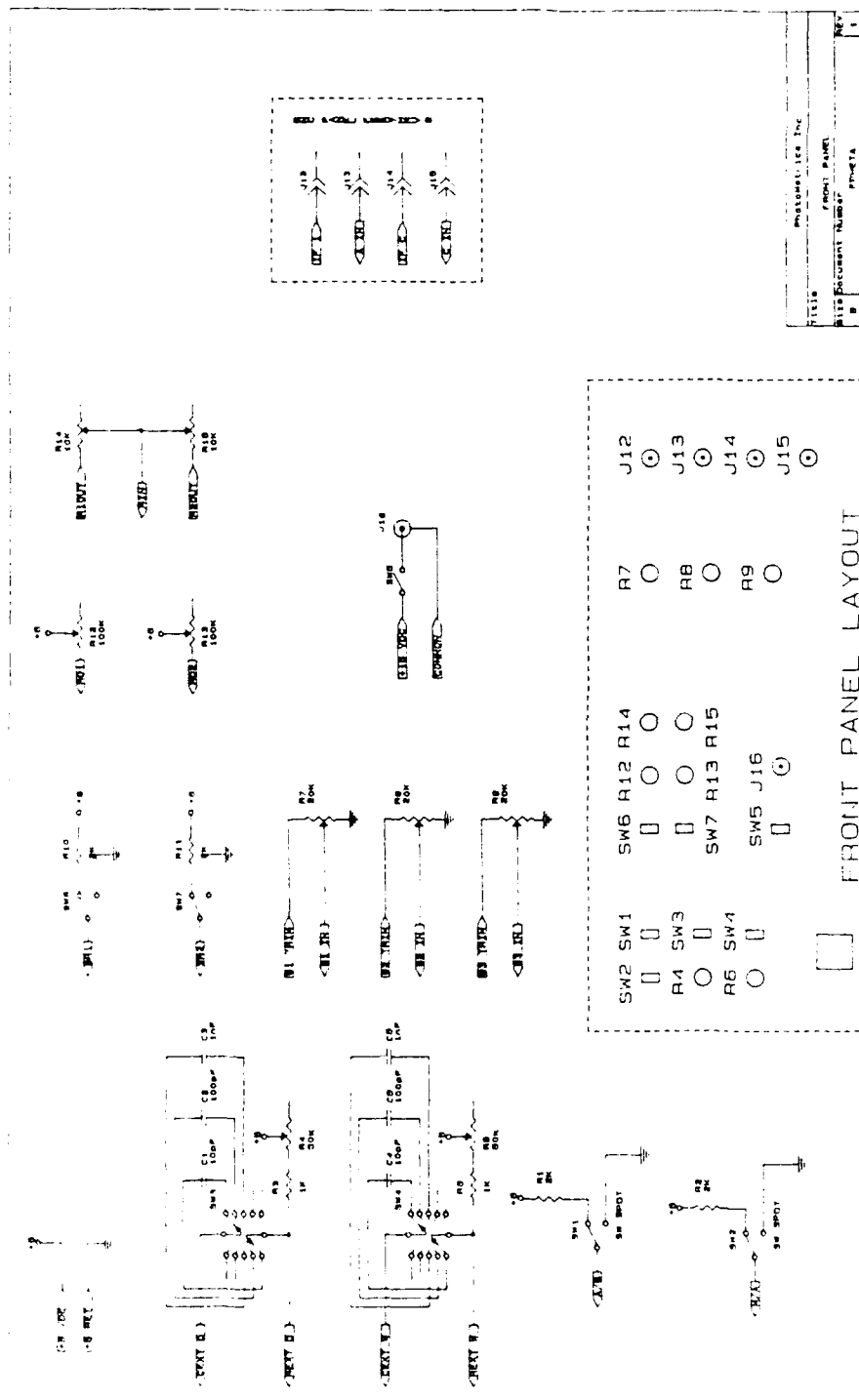


Figure 5.3.1c Amplifier unit: front panel schematic.

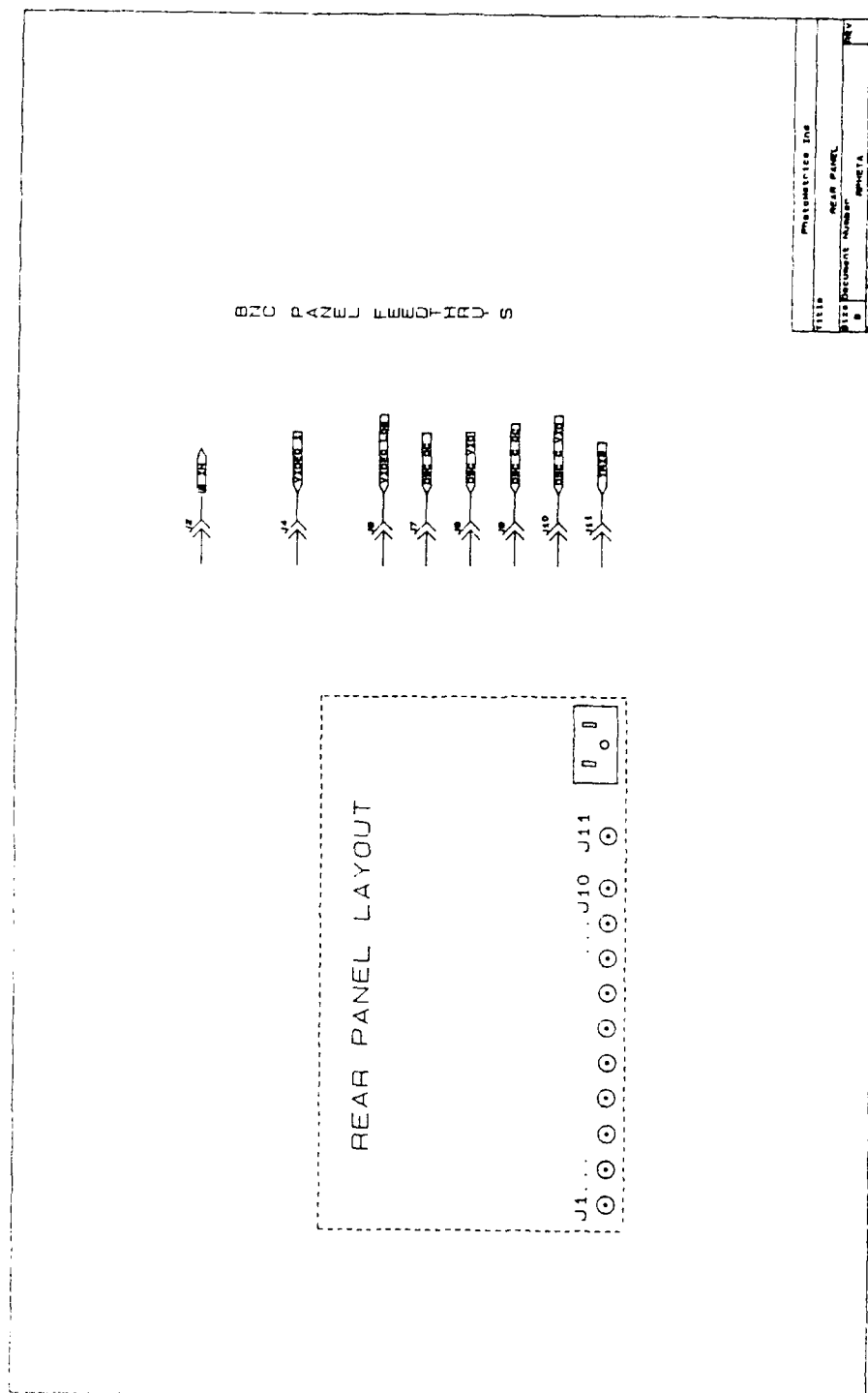


Figure 5.3.1d Amplifier unit: rear panel layout.

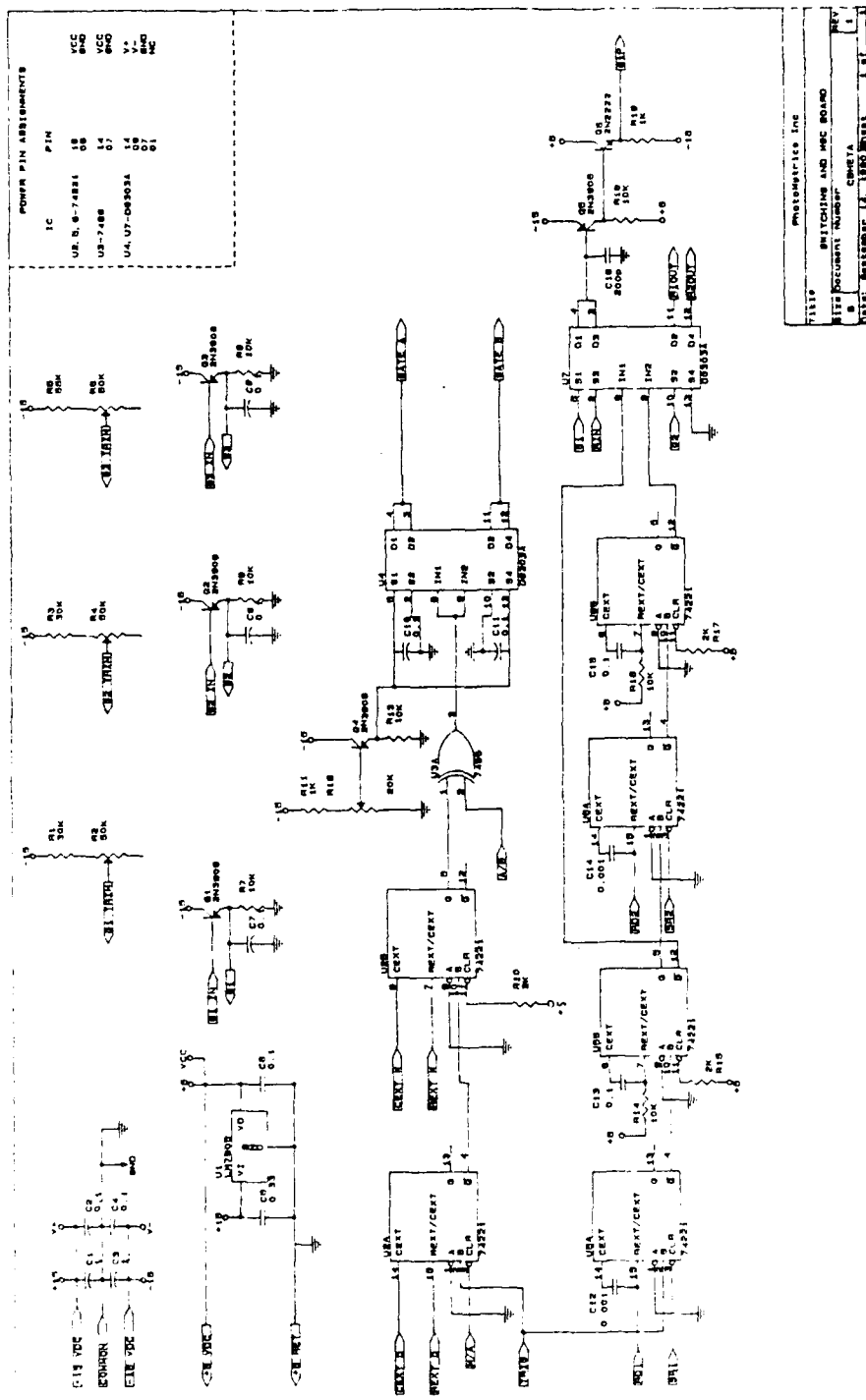


Figure 5.3.1e Amplifier unit: switching and MGC board schematic.

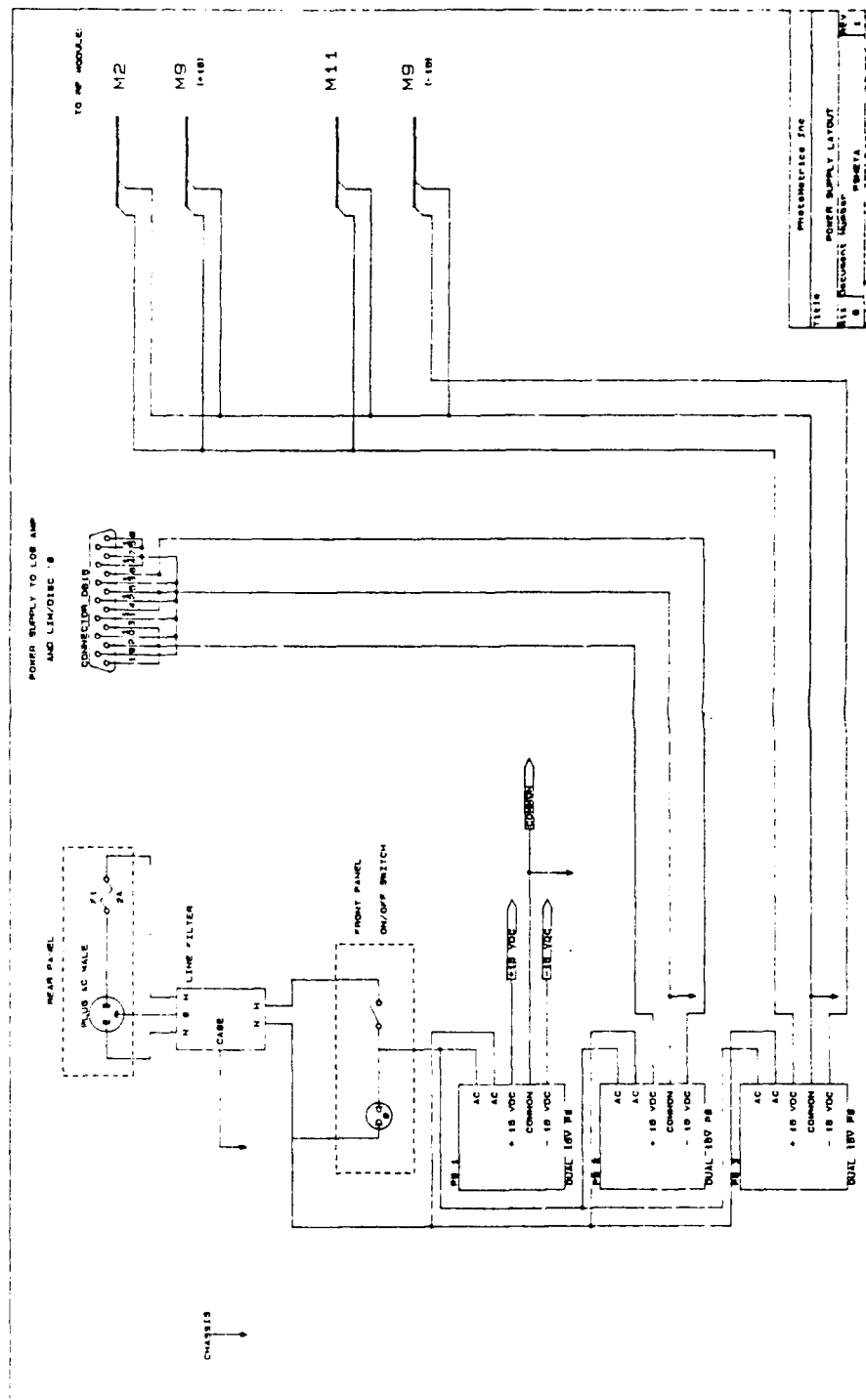


Figure 5.3.1f Amplifier unit: power supply circuitry.

The high gain channel was constructed for use with the preamplified heterodyne IF signal. This unit was specified to cover up to a 20 MHz bandpass about the IF center frequency (corresponding to a Doppler wind velocity range of ± 50 m/s). To obtain this coverage in a high gain linear amplifier it was necessary to first upconvert the signal center frequency to 70 MHz. As shown in figure 5.3.1b, this is done at M3 where the 40 MHz IF signal is mixed with a 110 MHz oscillator signal. The resultant signal--centered about 70 MHz-- is fed to a high gain amplifier whose bandpass is 30 MHz. Because the detector, added preamplifier, and shot noise powers are proportional to bandpass, optional filters are provided to reduce the amplifier input bandpass to 5 or 10 MHz. These are especially useful for increasing the signal to noise ratio in aerosol backscatter measurements where radial wind components above 12.5 or 25 m/s are not expected.

The signal source for this high gain channel can be switched manually or in response to a TTL trigger between a front panel (J15: source A) and a rear panel (J2: source B) connector. With the front panel gate mode switch, SW2, in the manual position (figure 5.3.1c), the source switch, SW1, selects between A and B. With auto mode and A(B) chosen, source A(B) will be normally selected with source B(A) gated. The B(A) selected gate period begins after a time delay--adjustable with pot R4 and range switch SW3--from the rising edge of the trigger pulse. The duration of the gate is adjustable using pot R6 and range switch SW4. This switching is done with a GaAs rf switch which is capable of switching times less than 5 nsec. In practice, we have found that switching transients can cause the downstream high gain amplifier to go into saturation with 1-10 μ sec recovery times.

We have also built-in a triggerable non-linear gain ramp in the high gain amplifier channel. With switch SW6 down (ramp off), the gain is manually controlled with knob R7. With switch SW6 up and SW7 down (ramp 1 on, ramp 2 off), the initial gain is set with R7 and the final gain with knob R8. The initial gain is held for a time after the rising edge of the trigger pulse. After this delay--adjustable with R12--the gain exponentially "relaxes" toward its final value with a time constant determined by R14. In dual ramp mode--both SW6 and SW7 up--the initial gain is set with R7 and an intermediate gain level with R8. The final gain is the maximum attainable with the amplifier. As in the single ramp mode, the initial gain is maintained for a time after the trigger pulse--controlled with R12--and then relaxes to the intermediate level with a

time constant adjustable with R14. After a second time delay from the commencement of this first ramp--adjustable with R13--the gain ramp time constant changes to one determined by R15 with relaxation towards the final--maximum--gain level. This operation is diagrammed in figure 5.3.2.

Although we have called this gain ramping exponential, it is actually the gain control voltage which is varying exponentially. Since the gain is a nonlinear function of this voltage, a non-exponential behavior versus time of the gain is expected. In addition, rapid gain variations are limited by the gain control response time of the RHG amplifier to about a 10 μ sec time constant. For setting of the ramp parameters (as well as calibrating gain versus time or range) we suggest using a constant power input to the amplifier at 40 MHz and monitoring the output on an oscilloscope.

5.4 Aerosol Signal Processing and Electronic Calibration

The arrangement used for aerosol backscatter measurements during the GABLE field program is illustrated in figure 5.4.1. The upconverted (to 70 MHz) and amplified IF signal is rectified by an HP rf detector diode. The resultant signal is digitized and averaged over a selectable number of lidar shots by a DSP 2112FS CAMAC module signal averager. The averaged waveform is passed to and recorded by the AST386 computer which controls the CAMAC crate. (On SABLE 89, a similar configuration was used but with the Analogic D6000 employed to digitize, average, and record the signal waveforms.)

The rf diode is roughly a square law detector for small signals (≤ -20 dBm) with rolloff towards linear response at higher input powers. Although this increases the dynamic range of the measurement, the nonlinearity (in power) must be corrected for before any data manipulation is done. To measure this response, we insert a known signal through a calibrated attenuator and into the diode. A generated pulse train is then used to trigger the signal averager. The recorded dc waveforms can later be used to determine rf power input versus recorded voltage. Figure 5.4.2 shows the results of such a measurement. The curve in this figure is a fifth order polynomial fit to the data. We have used this fitted polynomial to smoothly invert recorded voltage waveforms to rf power at the diode input.

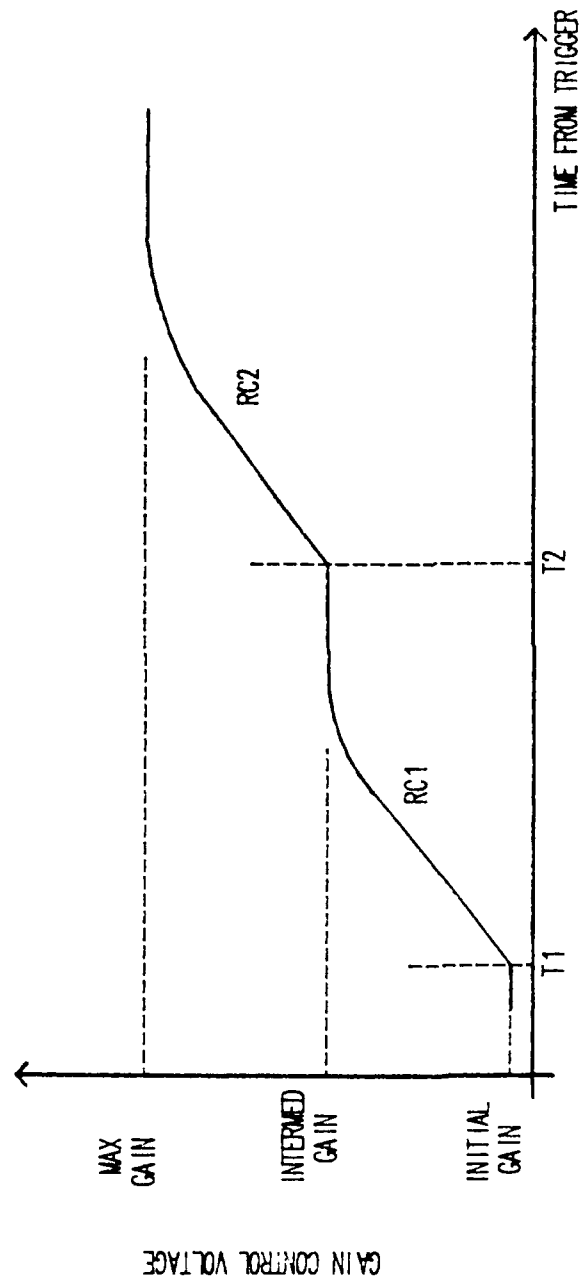


Figure 5.3.2 Amplifier unit: dual gain ramp operation.

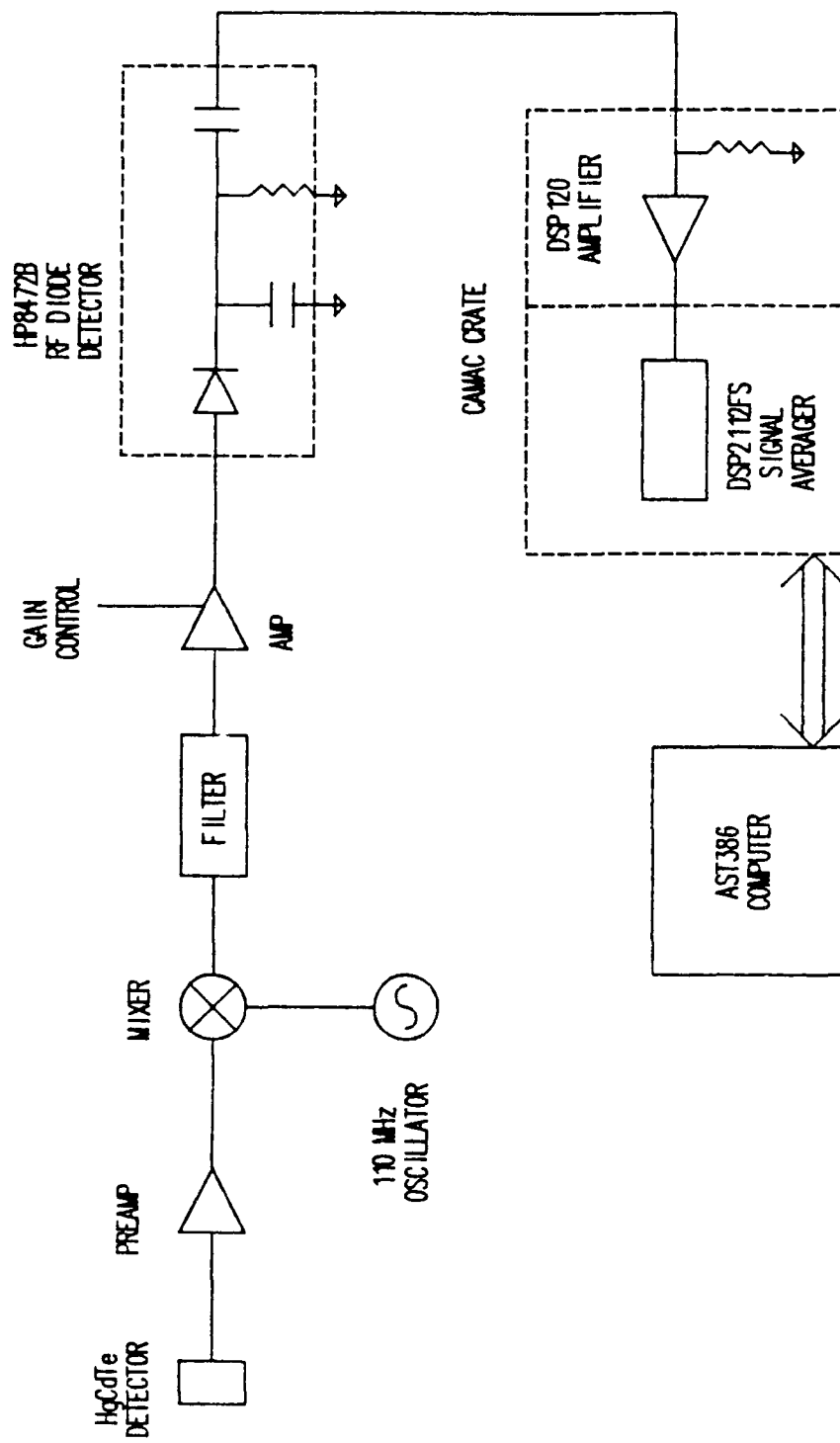


Figure 5.4.1 Block Diagram of receiver and data acquisition scheme.

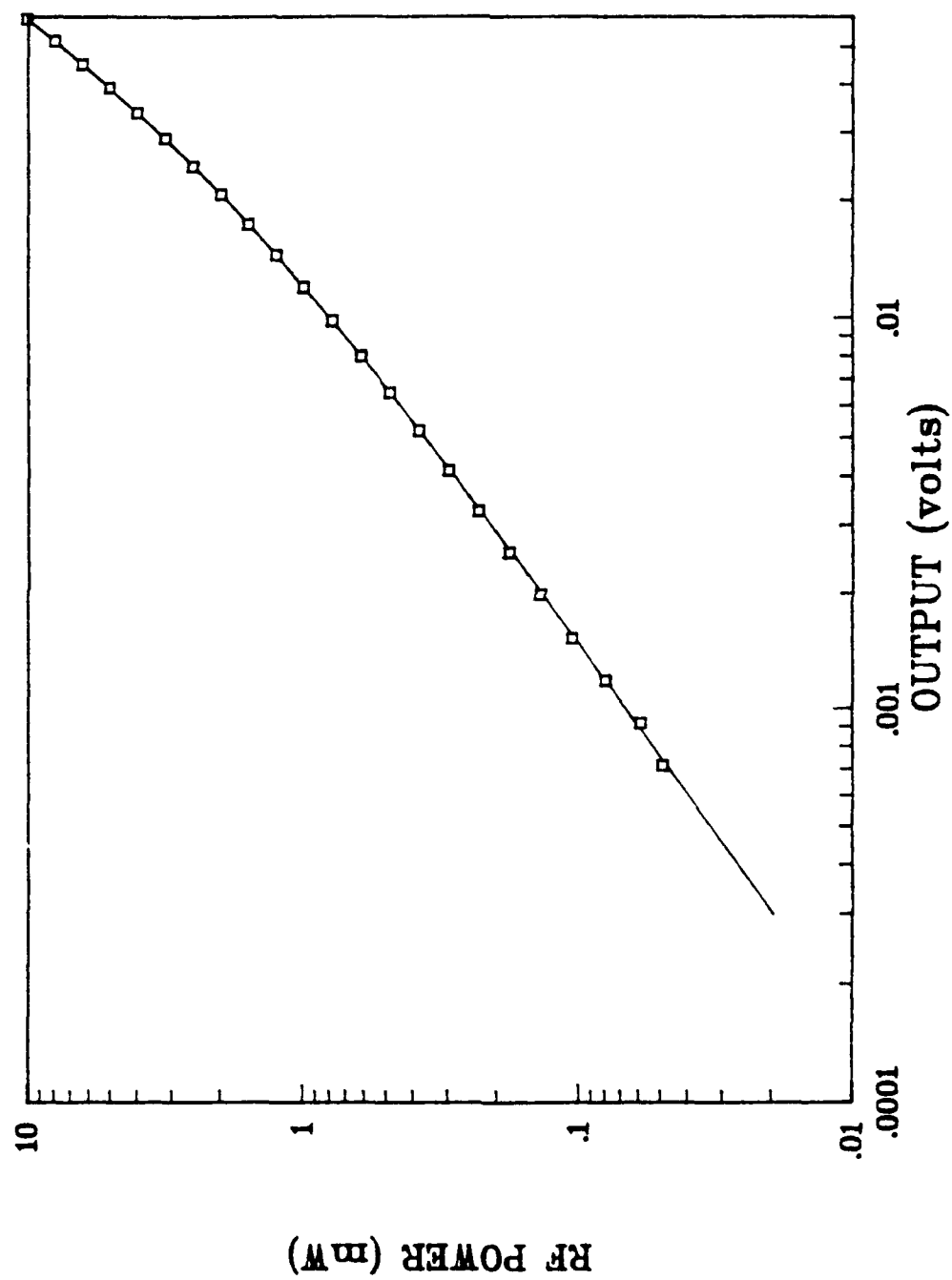


Figure 5.4.2 RF detector calibration.

5.5 Utility/Alignment Pyroelectric Detectors

We constructed two handheld detectors for use in aligning the expanded laser beam with the scanner mirrors and ensuring that the transmitted beam is striking the calibration target. The first was made for use inside the trailer with an oscilloscope and is wired for proportional response. For light pulses of duration less than about 10 μsec (as in this case) the output pulses are about 60 μsec long with a peak value proportional to the pulse energy striking the detector. The detector employed is a Molelectron P1-52 pyroelectric detector with a 2 mm diameter element and an Irtran window. The schematic for this detector is shown in figure 5.5.1.

The second detector was made for use in the vicinity of the calibration target to assist in lining up to the target. As oscilloscopes are difficult to handle and read in the field under daylight conditions, this unit was made to be self-contained with audible (beeper) and visual (LED) indications of the incidence of in-band, short duration radiation pulses. The schematic for this unit is shown in figure 5.5.2. The sensor element employed is a Molelectron P1-71 pyroelectric detector with a 1 mm element diameter. The output of the detector is AC coupled to a quad comparator to determine semiquantitatively the pulse energy range. The comparator outputs are pulse stretched and used to drive a bank of four LED's. A piezoelectric buzzer is driven in parallel with the most sensitive channel. External controls allow for deactivation of the buzzer and scaling of the sensitivity range.

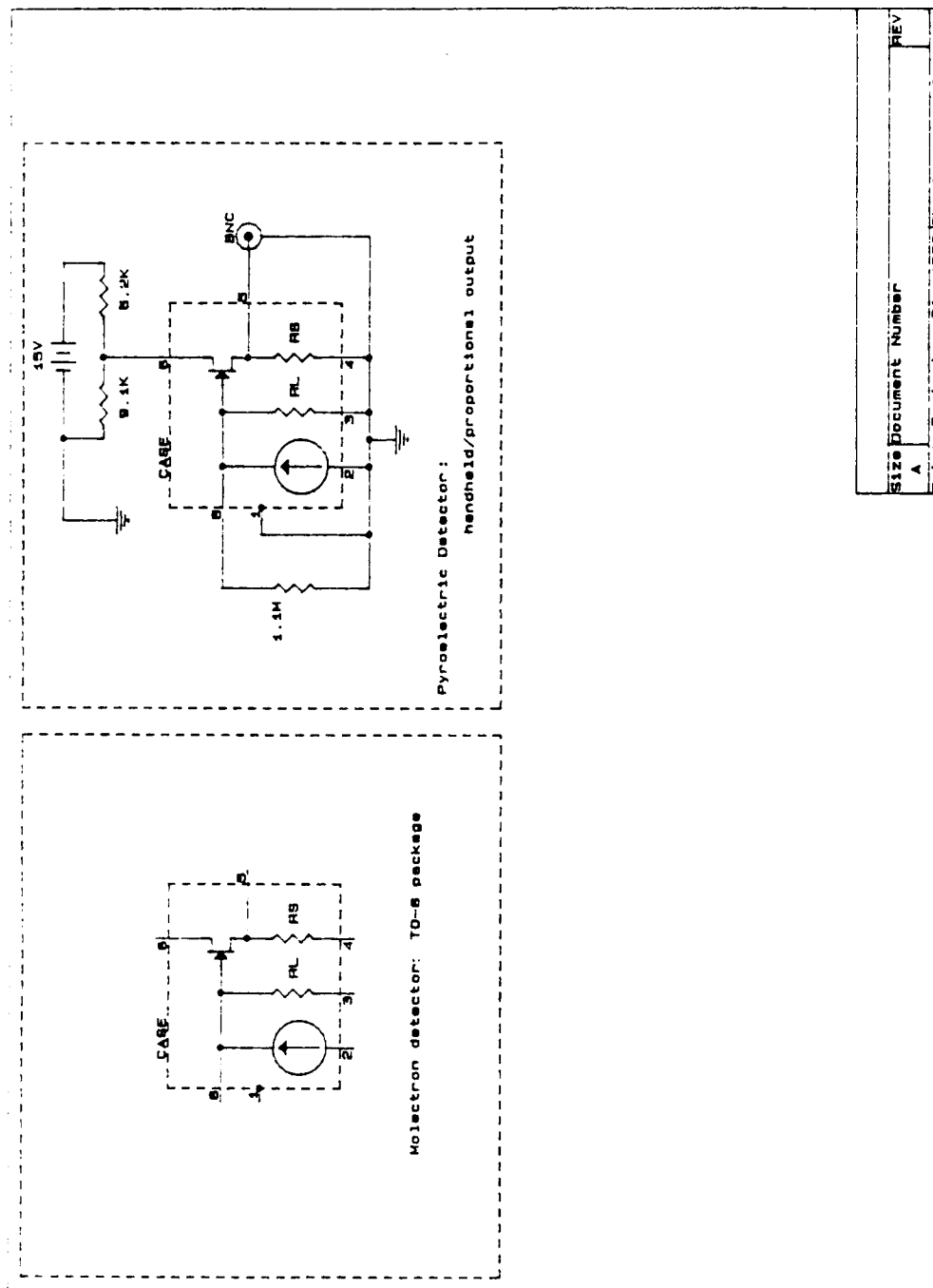


Figure 5.5.1 Schematic of the handheld proportional output detector.



59

6. CALIBRATION PROCEDURES

As noted in section 3.4, signal returns from a blue polystyrene target were used to calibrate the lidar to a known reference. We briefly discuss in this section the methods employed in the field to obtain target data as well as the analysis of these waveforms.

6.1 Field Techniques

The target used on the GABLE field measurement was a six foot square mounted at about a 45° angle to horizontal. (This angle is adjustable to enable compensation for possible elevation differences between the lidar and the target.) A significant off-normal angle is necessary to avoid specular reflection effects which are exhibited by this and most target materials. The reflectivity of the target material measured by JPL was at such a 45° angle of incidence.

Initial alignment of the lidar to the target was accomplished by eye using a coaligned HeNe laser. Our experience has shown that if care is taken in this coalignment, the HeNe and CO₂ beams will be separated by no more than about one to two feet over a path of up to 3.5 km. In particular, repeated measurements of the position of the HeNe and CO₂ beams at the turning mirror and the scanner aperture were found necessary to ensure a good alignment after the telescope. It was also found that verification of this alignment at a short range, about 50 to 100 meters from the trailer, was useful in reducing the time needed to locate the beam at several km ranges. The hand held pyroelectric detector was used to locate the CO₂ beam at both the near and far ranges.

For acquisition of the target data, the fastest digitizing rate (50 nsec per sample) afforded by the DSP2112FS signal averager was employed to obtain sufficient range resolution to characterize the return signal pulse. In addition, we used an rf gain about 25 to 30 dB lower than that for data collection since the relatively large signals from such hard targets would otherwise have saturated the amplifier.

Figure 6.1.1, shows the recorded signal for such a calibration run taken on 8/21/90 during the GABLE program. The signal amplitude here is that from the rf diode detector. Note the two signal artifacts at ostensible ranges of 0 and about 0.4

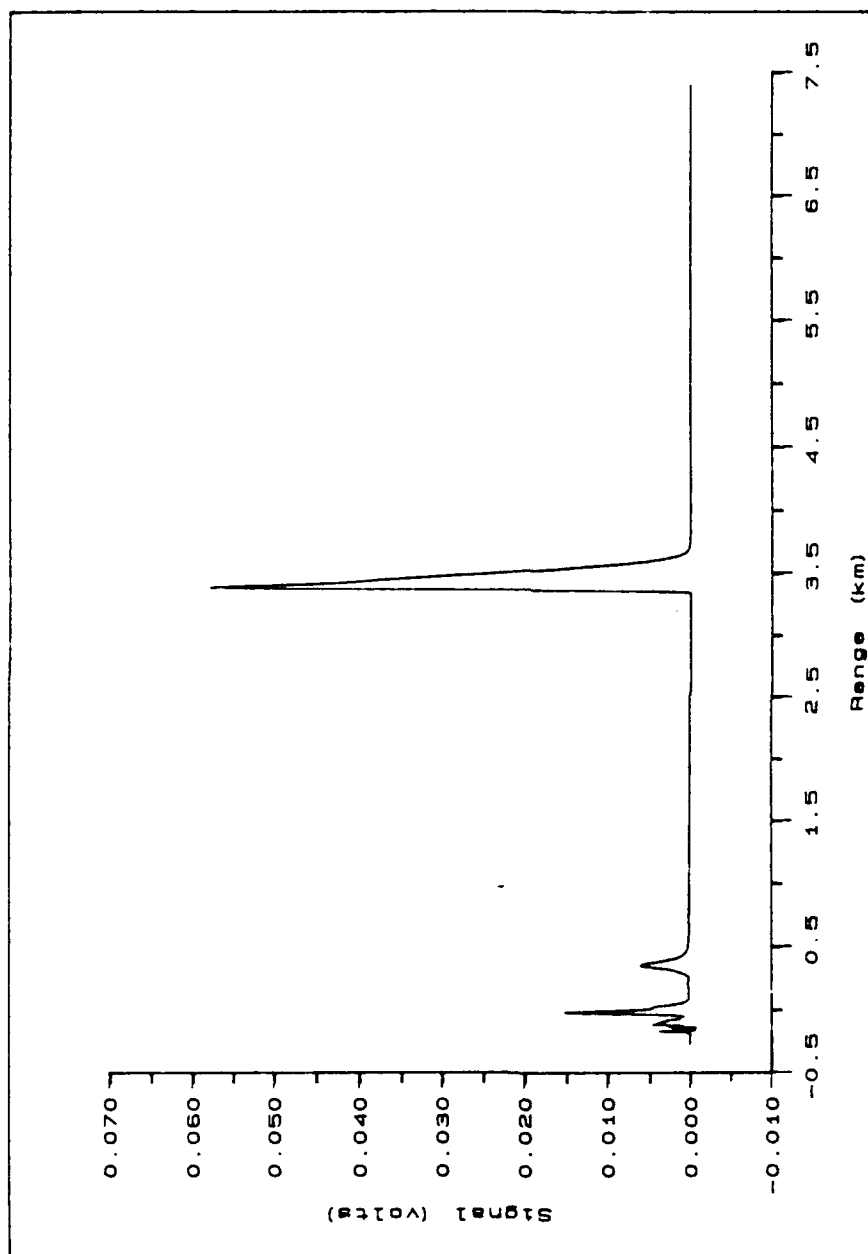


Figure 6.1.1 Sample target return data (AU210001).

km. The first is due to scatter from the transmission optics--rhomb, telescope, turning and scanner mirrors. The noise evident before this feature results from RF pickup from the laser triggering and firing circuits. The cause of the second artifact is not known but may be related to laser afterpulsing.

6.2 Preliminary Data Reduction

As discussed in section 5.4, the recorded signals must be corrected for the nonlinearity with power of the rf detector. Using the fit to the diode detector response discussed in section 5.4 and shown in figure 5.4.2, the signal can be converted from voltage to rf power referenced to the rf detector input. Figure 6.2.1 shows such a plot of IF signal power versus range for the same target calibration run as in figure 6.1.1. We have also divided out the measured amplifier gain (preamp and high gain) so that this plot is of the IF signal power at the output of the HgCdTe detector. Other than a change in scale, the only qualitative difference between the waveforms presented as rf power and those presented as detector voltage versus range is the enhancement in the former of the larger features due to compensation for the roll-off in the response of the diode rf detector.

Table 6.2.1 shows the results of this reduction for 12 consecutive target calibration runs taken on 8/21/90. In the third column, we have listed the total energy in the heterodyne signal pulse at the HgCdTe detector output. This was obtained by digitally integrating over the target return pulse. The average of this pulse energy (referred to as e_C in sections 2 and 3) over these 12 runs was used in section 3.5 to evaluate system sensitivity. The observed 14% variation in this quantity from run to run is greater than that expected due to laser power jitter or even target scintillation. (As noted in section 3.5, each run consists of the average of 100 laser shots.) It is possible that given the large range involved and the terrain along the sight path to the target that varying atmospheric conditions such as temperature and humidity were the cause of the observed variation in the magnitude of the target return.

The six runs listed at the bottom of table 6.2.1 were taken with a brownish Styrofoam packing material covering the target. The returns from this material were detectably smaller than from the blue polystyrene foam.

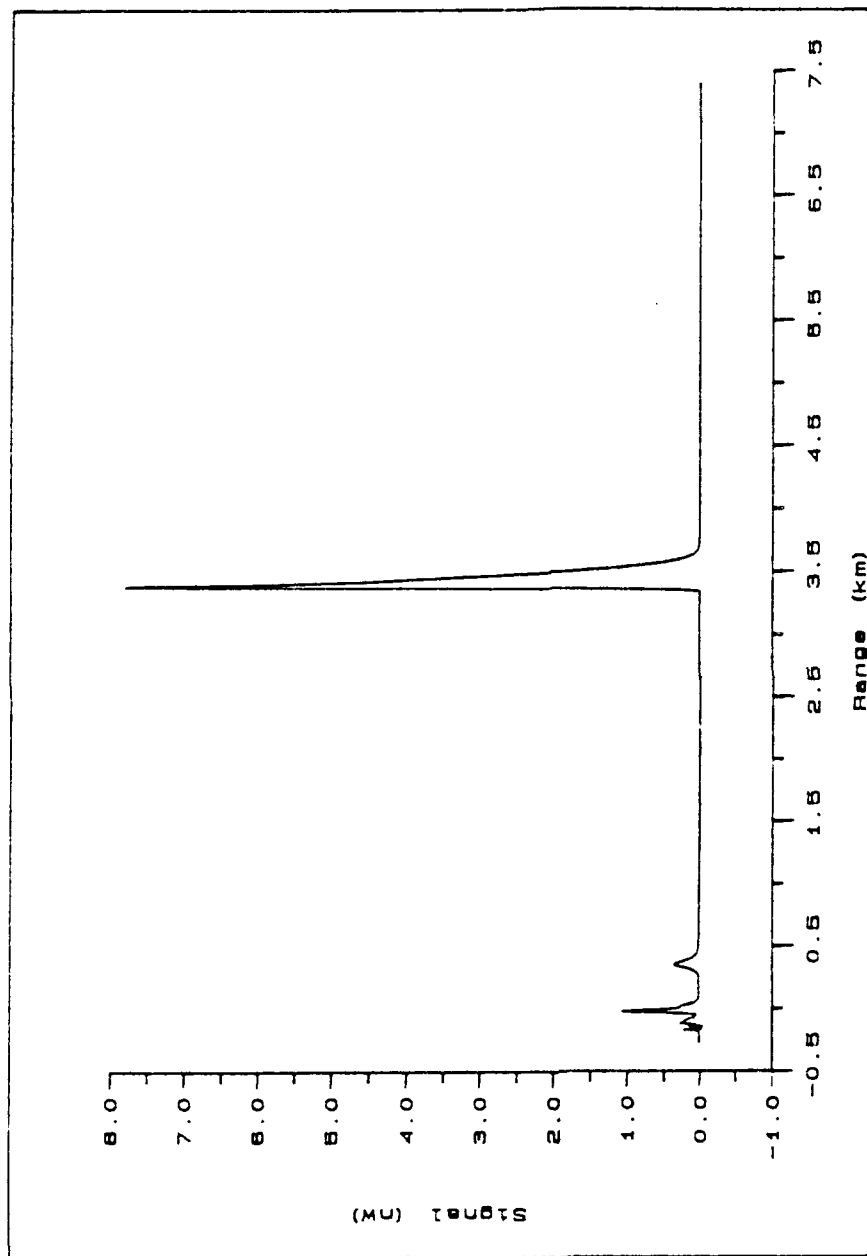


Figure 6.2.1 Reduced target return data: IF power versus range.

Figure 6.2.2 shows a similarly reduced data set taken on 8/20/90 with the lidar shooting along the valley and out toward the sea from Cinco Pico (the GABLE ground sight). This was taken concurrently with aircraft measurements along the valley. The feature at about 7 km range is a low lying cloud over the ocean.

TABLE 6.2.1

DATA RECORD	PEAK POWER 10^{-9} W	INTEGRATED RETURN 10^{-15} J
AU210001	7.80	4.69
AU210002	6.66	3.99
AU210003	6.81	4.22
AU210004	6.46	3.87
AU210005	6.78	4.07
AU210006	8.65	5.43
AU210007	6.24	3.78
AU210008	7.54	4.48
AU210009	7.92	4.77
AU210010	5.36	3.06
AU210011	7.73	4.67
AU210012	7.15	4.21
AU210013	5.10	3.00
AU210014	3.59	2.03
AU210015	3.72	2.18
AU210016	4.41	2.58
AU210017	3.02	1.68
AU210018	3.17	1.78

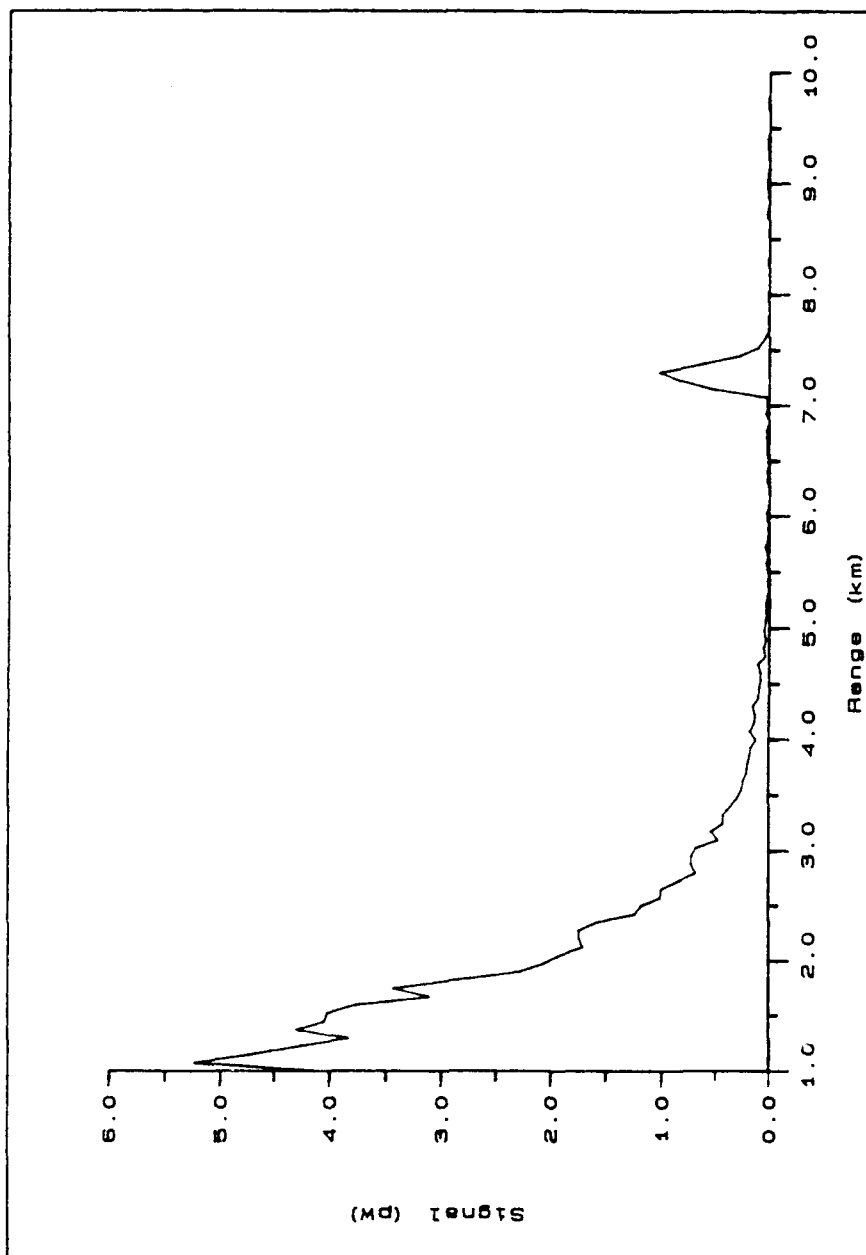


Figure 6.2.2 Reduced horizontal lidar run.

References:

- [2.1] C.M. Sonnenschein and F.A. Horrigan, "Signal-to-noise relationships for coaxial systems that heterodyne backscatter from the atmosphere," *Appl.Opt.* 10, 1600 (1971). L. Mandel and E. Wolf, "Optimum conditions for the heterodyne detection of light," *J.Opt.Soc.Am* 65, 413 (1974). D. Fink, "Coherent detection signal-to-noise," *Appl.Opt.* 14, 689 (1975). Y. Zhao, M Post, R. Hardesty, "Receiving Efficiency of monostatic pulsed coherent lidars. 1: Theory", *Appl.Opt.* 29, 4111 (1990).
- [2.2] O. Svelto, Principles of Lasers, Plenum, New York (1986).
- [2.3] D. Stoler, "Operator algebraic methods for laser cavity modes," in Coherence and Quantum Optics IV, L.Mandel and E. Wolf, eds. (Plenum, New York, 1978). D. Stoler, "Operator methods in physical optics," *J.Opt.Soc.Am.* 71,334 (1981).
- [2.4] A. Messiah, Quantum Mechanics, Wiley, New York (1958).
- [2.5] P.K. Cheo, Fiber Optics and Optoelectronics, Prentice Hall, New Jersey 1990.
- [2.6] H.H. Hopkins, "The concept of partial coherence in optics," *Proc.Roy.Soc.* A208, 263 (1951).
- [3.1] J.T. Cox, G. Hass, W.R Hunter, "Infrared reflectance of silicon oxide and magnesium fluoride protected aluminum mirrors at various angles of incidence from 8 to 12 μm ", *Appl.Opt.* 14, 1247 (1975). S.F. Pellicori, "Infrared reflectance of a variety of mirrors at 45° incidence," *Appl.Opt.* 17, 3335 (1978).
- [3.2] F.X. Kneizys et al., Atmospheric Transmittance/Radiance: Computer Code LOWTRAN 6, AFGL-TR-83-0187, August 1983, ADA137786.
- [3.3] R. McClatchy and J. Selby, Atmospheric Attenuation of Laser Radiation from 0.76 μm to 31.25 μm , AFCRL-TR-74-0003, January 1974, ADA779726.
- [3.4] M. Kavaya, R. Menzies, D. Haner, U. Oppenheim, and P. Flamant, "Target reflectance measurements for calibration of lidar atmospheric backscatter data," *Appl. Opt.* 22, 2619 (1983). H. Henshall and J. Cruickshank, "Reflected characteristics of selected materials for reference targets for 10.6 μm laser radars," *Appl.Opt.* 27, 2748 (1988). D. Haner and R. Menzies, "Reflectance

- characteristics of reference materials used in lidar hard target calibration," Appl.Opt. 28, 857 (1989).
- [3.5] Private communication, D. Haner (JPL) to M.Sgt. K. Wolfe.(GL/OPA).
- [3.6] M. Born and E. Wolf, Principles of Optics, 6th Ed. (Pergamon, New York, 1986). J. Simmons and M. Guttman, States, Waves and Photons, (Addison Wesley, Reading, MA, 1970).
- [5.1] J. Smith, Modern Communications Circuits, (McGraw-Hill, New York, 1986).
- [5.2] K. Ma, F.F. Hall, R.M. Hardesty, T.R. Lawrence, and R.E. Cupp, "Heterodyne quantum efficiency of a HgCdTe infrared Doppler detector," Appl.Opt. 28, 1750 (1989).
- [5.3] G.B. Jacobs, Pulsed Heterodyne CO2 Laser/Scanner System, AFGL-TR-83-0191(I), June 1983, ADA135059.